Correspondence:

# A generalized photon-tracking approach to simulate spectral snow albedo and ~~transmissivity~~ transmittance using ~~x-ray~~ X-ray microtomography and geometric optics

Theodore Letcher[1], Julie Parno[1], Zoe Courville[1], Lauren Farnsworth[1], and Jason Olivier[1]

[1]US Army Corps of Engineers Cold Regions Research and Engineering Laboratory,Hanover, NH

**Correspondence:** Theodore Letcher (Theodore.W.Letcher@erdc.dren.mil)

**Abstract.**

A majority of snow radiative transfer models (RTM) treat snow as a collection of idealized grains rather than ~~a semi-organized~~ an organized ice-air matrix. Here we present a generalized multi-layer photon-tracking RTM that simulates light ~~transmissivity and reflectivity through~~ reflectance and transmittance of snow based on ~~x-ray microtomography~~ X-ray microtomography images, treating snow as a coherent structure rather than a collection of grains. ~~Notably, the~~ The model uses a blended approach to expand ray-tracing techniques applied to sub-1 cm³ snow samples to snowpacks of arbitrary depths. While this framework has many potential applications, this study's effort is focused on simulating ~~light transmissivity~~ reflectance and transmittance in the visible and near-infrared (NIR) through thin snowpacks as this is relevant for surface energy balance ~~applications and sub-nievean hazard detection~~ and remote sensing applications. We demonstrate that this framework fits well within the context of previous work and capably reproduces many known optical properties of a snow surface, including the dependence of spectral reflectance on snow ~~grain size~~ specific surface area and incident zenith angle ~~and the surface bidirectional reflectance distribution function~~ as well as the surface Bidirectional Reflectance Distribution Function (BRDF). To evaluate ~~how the model simulates transmissivity~~ the model, we compare it against ~~spectroradiometer measurements collected~~ reflectance data collected with a spectroradiometer at a field site in east-central Vermont. In this experiment, painted panels were inserted at various depths beneath the snow to emulate thin snow. The model compares remarkably well against the ~~spectroradiometer measurements~~ reflectance estimated from the spectroradiometer measurements, with an RMSE of 0.03. Sensitivity simulations using this model indicate that snow ~~transmissivity~~ transmittance is greatest in the visible wavelengths~~and is limited~~, limiting light penetration to the top ~~5~~ 6 cm of the snowpack for ~~fine-grained snow , but can penetrate as deep as 8 cm for coarser~~ fine grain snow but increasing to 12 cm for coarse grain snow. ~~An evaluation of snow optical properties generated from a variety of snow samples suggests that coarse grained low density snow is most transmissive~~ These results suggest that the 5% transmission depth in snow can vary by over 6 cm according to the snow type.

# 1 Introduction

Due to the highly reflective nature of snow, seasonal snowpacks make the surface significantly more reflective when present, impacting regional weather and climate. Correspondingly, the snow albedo feedback, caused by changes in seasonal snow cover extent and properties, represents one of the more dramatic markers of regional and global climate change (e.g., Hall, 2004; Déry and Brown, 2007; Flanner et al., 2011; Letcher and Minder, 2015; Thackeray and Fletcher, 2016). While snow is highly reflective, snow albedo is not equal for all snowpacks. For instance, snow albedo typically decreases with snow age due to metamorphic processes resulting in larger snow grains (e.g., Wiscombe and Warren, 1980; Aoki et al., 2000; Flanner and Zender, 2006; Adolph et al., 2017). Snow albedo is also diminished by light absorbing impurities such as dust or black carbon that contaminate the snow ~~(e.g., Doherty et al., 2010; Painter et al., 2012; Skiles et al., 2012; Dumont et al., 2014; Skiles et al., 2015; Skiles and Painter, 20~~ Importantly, these two effects impact different parts of the electromagnetic spectrum, with grain size having a greater influence in the near-infrared (NIR), and the particle contamination influencing the visible region. Finally, even though thin snow covers are highly reflective, the ~~aggregate~~ surface albedo for a thin snow cover can be influenced by the underlying ground surface depending on the snow microstructure (Perovich, 2007; Warren, 2013; Libois et al., 2013). Consequently, the detection of subnivean hazards is highly dependent on the microscopic properties of the overlaying snowpack. Understanding these small-scale drivers of snow albedo is important for large-scale remote sensing applications and regional weather and climate modeling.

There are several documented approaches to ~~modeling~~ model snow broadband and spectral albedo using radiative transfer models (RTMs) in efforts to better understand and predict the effects of snow aging and impurities on snow optical properties. While a full review of snow radiative transfer is well beyond the scope of this paper, we refer the reader to He and Flanner (2020) for a rigorous overview of the different approaches. There are also numerous simplified parameterizations for snow albedo of varying complexity designed for implementation in weather and climate models (e.g., Verseghy, 1991; Dickinson, 1993; Gardner and Sharp, 2010; Vionnet et al., 2012; Saito et al., 2019; Bair et al., 2019).

At a fundamental level, the scattering of electromagnetic energy incident upon the boundary separating a snow grain and the surrounding air is determined by the different refractive indices for ice and air and the geometry of the interfaces. The absorption of light as it passes through solid ice is well understood and has a strong wavelength dependence ~~(e.g., Grenfell and Perovich, 1981; Perovic~~ The scattering of visible and NIR light at an air/ice boundary is well described by the geometric optics approximation, ~~which requires that the wavelength of light is~~ where the wavelengths of visible and NIR light are small relative to the size of the ~~scattering particle~~ typical snow particle (e.g., Kokhanovsky and Zege, 2004). While the physics behind scattering and absorption are well understood ~~for a single snow particle~~ within the geometric optics limit, the actual path of a light ray through a snowpack can be extraordinarily convoluted as the ray is constantly intersecting air/ice interfaces with very little absorption.

Seminal studies describing snow albedo modeling (e.g., Warren and Wiscombe, 1980; Wiscombe and Warren, 1980) and most subsequent approaches treat snow grains as independent scatterers, where the scattering properties of an individual grain are not affected by adjacent grains and are independent of the spacing between grains and, thus, snow density. ~~Mie theory is typically used to calculate snow albedo owing to its computational efficiency(e.g., Bohren and Beschta, 1979; Wiscombe, 1980).~~

~~However~~For simplification and computational efficiency, Mie theory is ~~most often applied to particles with spherical geometries, and so it is common practice to represent snow by~~ often used to determine the albedo of snow represented as a collection of ~~effective spheres~~spherical particles (e.g., Bohren and Beschta, 1979; Wiscombe, 1980). Yet although snow grain size is often

60 most cited as the key driver of ~~pure~~ snow albedo, grain shape also has an impact~~on snow spectral albedo (Aoki et al., 2000; Libois et al., 201~~ ~~For instance, an inter-comparison of several commonly-used two stream RTMs parameterizing snow grains as equivalent spheres conclude that these models overestimate snow albedo in the NIR (Dang et al., 2019).~~

, leading to inaccuracies with the spherical assumption (Aoki et al., 2000; Neshyba et al., 2003; Picard et al., 2009; Libois et al., 2013; D

Efforts to understand and simulate the impacts of snow particle shape on snow spectral albedo have largely focused on lever-

65 aging the geometric optics approximation in various ways. For instance, Yang and Liou (1996) used ray-tracing to compute the single scattering properties of idealized hexagonal columns, plates, and rosettes. Grundy et al. (2000) presented a Monte Carlo approach to estimate optical properties of computer-rendered 3D spheres that compared well with Mie theory. Their work was extended to estimate the scattering properties of irregularly shaped crystals. ~~A more recent effort~~

Recently, there have been numerous efforts to characterize snow as a coherent medium rather than a collection of particles

70 within the context of radiative transfer. For instance, Malinka (2014) combined stereological techniques and geometric optics to obtain the inherent optical properties of a snowpack. An additional study by Xiong et al. (2015) focused on determining the optical properties of an idealized mixed snow/air medium generated from a randomized bicontinuous 2D representation of the snow. ~~More recently, several studies have used ray-tracing and photon-tracking methods to simulate snow optical properties from renderings of snow particles generated from~~ X-ray microtomography (hereby: $\mu$CT) ~~scans of real snow~~

75 ~~(Haussener et al., 2012; Kaempfer et al., 2007; Ishimoto et al., 2018; Dumont et al., 2017).~~

is a powerful tool that has been used in many of these medium-based efforts. $\mu$CT has been used to support numerous snow radiative transfer methods including individual particle scattering, ray-tracing, and analytical approaches (Haussener et al., 2012; Kaempfer

Collectively, RTM-focused studies of snow have greatly expanded the knowledge surrounding the optical properties of irregular snow grains and informed the role of snow microstructure on spectral reflectance ~~. However, the impact of snow microstructure~~

80 ~~on snow spectral transmissivity has often been overlooked in observations and modeling~~and transmittance.

In this study, we build upon the approaches of Grundy et al. (2000), Kaempfer et al. (2007), Jacques (2010), and Xiong et al. (2015) to develop a Monte Carlo photon-tracking snow RTM that ~~is driven by~~ focuses on representing snow as coherent 3D structure rather than a collection of particles. This framework employs ray-tracing to simulate photon tracks through 3D renderings of snow samples measured using $\mu$~~CT observations of snow~~ CT and is designed for broad applications, including

85 ~~snow transmissivity. The primary purpose of this RTM framework is to use explicit photon-tracking techniques in conjunction with 3D renderings of snow samples to estimate realistic snow optical properties for use in a Monte Carlo photon-tracking model~~studying the effects of snow type and snow depth on snow spectral albedo and transmittance in the visible and NIR. In section 2, we describe the model framework and $\mu$CT data processing. In section 3, we demonstrate the model's capability to reproduce known optical properties of snow, compare model output to spectral albedo measurements of objects buried beneath

90 snow at various depths, and use the RTM to investigate snow ~~transmissivity~~transmittance. In sections 4 and 5, we present a broad discussion and conclusions.

## 2   Data and Methods

~~Here we describe the framework of a new,~~

The RTM framework used here is divided into two distinct components. The first determines key snow optical properties by firing photons into 3D closed-surface renderings of snow samples derived from $\mu$CT scans with a voxel resolution of $\approx 20~\mu m$. The second is a semi-quantized ~~Monte Carlo photon-tracking model designed to simulate radiative transfer (RT) through snow with a focus on~~ 1D plane-parallel Monte Carlo model that uses the optical properties derived from the first part.

In the plane-parallel model, individual photon packets are initialized at the snow surface with a prescribed incident direction into the snowpack. Then, each packet has a unique path whereby all of the energy contained within a given packet travels in the same direction and the amount of energy within a given packet is depleted continuously according to absorption within the medium. The plane-parellel model is used to simulate spectral albedo and ~~transmissivity~~ transmittance in the visible and NIR (i.e., ~~$380 \leq \lambda \leq 1300$ nm) .~~ $380 \leq \lambda \leq 1600$ nm) for snowcovers with arbitrary depths and known lower boundaries. In both model components, the ice refractive indices reported by Warren and Brandt (2008) are used to compute scattering and absorption.

While computationally expensive, there are several advantages to the Monte Carlo approach~~over more traditional approaches that aim to solve the radiative transfer equation (RTE)~~. In particular, Monte Carlo models are useful for modeling ~~RT through~~ single scattering properties of non-spherical particles and for 3D ~~RT~~ radiative transfer applications (e.g., Iwabuchi, 2006; Whitney, 2011). ~~In this model, the Monte Carlo approach is used in order to eliminate all assumptions regarding snow microstructure. Specifically, this approach treats the snowpack more as a coherent structural ice lattice rather than as a collection of idealized particles. The explicit photon-tracking through 3D renderings of snow performed as part of this model are similar to those described in Grundy et al. (2000); Kaempfer et al. (2007); Dumont et al. (2017); Ishimoto et al. (2018).~~ Additionally, the Monte Carlo approach lends itself well to parallelization, and the semi-quantized approach described here reduces the number of photons required to achieve a statistically robust result. ~~Yet, this approach is not without its drawbacks. For instance, the geometric optics approximation localizes the ray, directing all scattered radiation along a single path. Further, this framework ignores the~~

One critical simplification we make in this model is that we ignore the wave properties of light, such as phase and diffraction, which limits its overall applicability and ~~reducing accuracy. Despite these drawbacks, numerous approaches in~~ reduces accuracy. However, this simplification has been used successfully in numerous previous studies (e.g., Kaempfer et al., 2007; Malinka, 2014; because the diffraction pattern is strongly forward scattering (Xiong et al., 2015), we anticipate that this simplification is appropriate here. While some work has been done incorporating diffraction into geometric optics scattering for non-spherical particles (Yang and Liou, 1996; Liou et al., 2011), because this framework treats snow as a two-phase medium rather than a collection of particles, accounting for diffraction is less straightforward. Accordingly, we acknowledge that diffraction may be more important for the ~~literature have demonstrated success in simulating snow reflectance of natural (i.e., unpolarized) light using these simplifications (e.g., Kaempfer et al., 2007; Malinka, 2014; Xiong et al., 2015).~~

125    ~~This model can be divided into two distinct components. The first of which determines key snow medium optical properties by launching photons into 3D closed-surface renderings of snow samples derived from $\mu$CT scans with a voxel resolution of $\approx 20~\mu$m. The second uses the optical properties derived from the first part to drive a 1D photon-tracking model whereby individual photon packets are prescribed a random initial position and incident direction on the snow. Each individual photon packet then has a unique path whereby all of the energy contained within a given packet travels in the same direction and the~~

130 ~~amount of energy within a given packet is depleted continuously according to absorption within the medium. Note that for both model components, the ice refractive indices reported by Warren and Brandt (2008) are used to compute scattering and absorption~~longer NIR wavelengths, and should be a potential focus of future work.

## 2.1   Snow Optical Properties

   The ~~1D medium~~ plane-parallel model requires three key optical properties: the extinction coefficient ($\gamma_{ext}$ [mm$^{-1}$]), the mean

135 path fraction traveled within ice ($F_{ice}$), and the scattering phase function (~~$p(cos\Theta)$~~$p(\cos\Theta)$). In considering ~~light as a ray~~ a photon of light traveling through the snow medium ~~, which is scattered each time it intersects~~ along a path, the photon is considered extinct when it intersects and is scattered along an air/ice boundary ~~and partially~~ or is absorbed within the ice~~, the~~. The extinction coefficient is ~~related to the~~ then inversely proportional to the mean distance traveled between these scattering and absorption events. The phase function determines the change in direction of the ray during a scattering event, and the

140 ice-path fraction, when combined with the spectrally variable ice absorption coefficient ($\kappa(\lambda)$), determines the mean energy depleted from the ray for a given distance traveled between scattering events. ~~For a given snow sample~~In this model, $\gamma_{ext}$ is determined for a given snow sample following the method described in Xiong et al. (2015)~~applied to the 3D rendering of snow as opposed to an idealized bicontinuous medium~~. In this framework, photons are initialized at a random position within the snow sample, and launched in a random direction for a specified distance ($L$). If the photon is initialized within the air,

145 the probability of extinction ($P_{ext}$) is 1 if a boundary is intersected over $L$, otherwise it is 0. In the case where the photon is initialized within the ice medium, $P_{ext}$=1 if a boundary is intersected over $L$, otherwise it is given as:

$$P_{ext} = 1 - e^{-\kappa_\lambda L}, \tag{1}$$

   where $\kappa_\lambda$ is the wavelength-dependent absorption coefficient of ice, which is related to the imaginary part of the ice refractive index ($k$):

150   $$\kappa_\lambda = \frac{4\pi k}{\lambda}. \tag{2}$$

   This slight modification is made to account for the added probability of extinction due to absorption of the photon within the ice particle. ~~Note that this also introduces a minor wavelength dependence into the extinction coefficient.~~ Using this method, a probability of extinction can be determined for distance $L$. This method is repeated for several distances ranging from the voxel resolution (20 $\mu$m) to the width of the snow sample volume (e.g., 10 mm). The extinction coefficient is then determined

155 using a curve fit to the Beer-Lambert law:

$$P_{ext} = 1 - e^{-\gamma_{ext} L},\qquad(3)$$

The mean fractional ice path ($F_{ice}$) is determined by tracking individual photons as they travel throughout the ~~aggregate~~ snow sample. This framework closely mimics that of Kaempfer et al. (2007) in that photons travel through the snow medium and change direction according to Snell's law of refraction and a probabilistic representation of Fresnel's law of reflectance. Here, a photon is initialized at a random starting point somewhere ~~within~~ along an edge of the snow sample and launched in a random direction into the snow sample. The photon is tracked until it exits the medium, and the $F_{ice}$ is ~~simply~~ the ratio of the distance traveled within ice ~~over~~ and the total distance traveled. This is repeated for a large number of photons to determine an average $F_{ice}$.

Fresnel's law dictates that the fractional reflection and transmission of light at a boundary is related to the incident angle ($\theta_i$) and the refractive indices ($n$) of the two media separated by the boundary:

$$R_h = \frac{n_1 \cos\theta_i - n_2\sqrt{1 - \left(\frac{n_1}{n_2}\sin\theta_i\right)^2}}{n_1 \cos\theta_i + n_2\sqrt{1 - \left(\frac{n_1}{n_2}\sin\theta_i\right)^2}},\qquad(4)$$

and

$$R_v = \frac{n_1\sqrt{1 - \left(\frac{n_1}{n_2}\sin\theta_i\right)^2} - n_2\cos\theta_i}{n_1\sqrt{1 - \left(\frac{n_1}{n_2}\sin\theta_i\right)^2} + n_2\cos\theta_i},\qquad(5)$$

where $R_h$ and $R_v$ are the horizontally and vertically polarized reflectances. Assuming that the radiation is unpolarized (e.g., natural light), the reflectance ($R$) is:

$$R = \frac{1}{2}\left(R_h^2 + R_v^2\right).\qquad(6)$$

Through energy conservation, the transmittance ($T$) is ~~simply~~:

$$T = 1 - R.\qquad(7)$$

Then, if the vector normal to the boundary plane ($\hat{v}_n$) is oriented towards the medium with refractive index $n_1$, the direction unit vectors for ~~transmitted and reflected~~ reflected and transmitted radiation are computed as ($\hat{v}_r$) and ($\hat{v}_t$):

$$\hat{v_r} = \hat{v_i} + 2\cos\cos\theta_i \hat{v_n} \tag{8}$$

and

$$\hat{v_t} = \frac{n_1}{n_2}\hat{v_i} + \left(\frac{n_1}{n_2}\cos\cos\theta_i - \cos\cos\theta_t\right)\hat{v_n}, \tag{9}$$

where $\hat{v_r}$ and $\hat{v_t}$ are the reflection and transmission unit direction vectors, respectively. We note that $F_{ice}$ is determined by both the density of snow and the prevalence of internal reflections and, accordingly, is related to the absorption enhancement parameter $B$ described in Kokhanovsky and Zege (2004). $B$ quantifies the absorption path length extension due to internal reflections within a snow particle, and can be quantified by the ratio of the actual internal photon path-length through a sample medium and the internal path-length following a straight line (Libois et al., 2019). In this study we compute $B$ for each snow sample following this method for comparison against previous work (Kokhanovsky and Zege, 2004; Libois et al., 2014).

The phase function is determined by separating out individual snow grains from the reconstructed 3D snow sample and probing them with photons to compute the scattering angle In this framework, the phase function represents localized scattering at an air/ice interface as is done in Haussener et al. (2012) and Xiong et al. (2015). Here, the phase function is determined by tracking scattering angles during the algorithm used to determine $F_{ice}$. During this procedure, the phase function is first divided into a prescribed number of finite bins ($j$) with width, $d\Theta$. Each time a photon intersects an air/ice boundary the scattering angle is computed for both the reflected and transmitted directions where the cosine of the scattering angle ($\Theta$) is the dot product between the directional unit vector of radiation incident on the particle boundary ($\hat{\Omega}'$) and the directional unit vector of the scattered radiation ($\hat{\Omega}$) in the cartesian Cartesian coordinate space:

$$\cos\cos\Theta = \hat{\Omega}' \cdot \hat{\Omega}. \tag{10}$$

The phase function is constructed by first initializing a photon outside of a given particle and firing it in a random direction towards the particle. The photon then interacts with the snow particle, guided by Eqs. 4 - 9. For each collision ($i$), the amount of energy exiting the particle into the directional bin ($cos\Theta_j$) is tracked, and the remaining photon energy is depleted as energy exits, or is absorbed within, the ice particle. This is repeated for an arbitrary number of collisions ($n$) until there is less than 0.1% of the initial energy left (Fig. 1). For the initial collision ($i = 0$), the energy exiting the particle is simply the reflected fraction of the incident ray, and for each subsequent collision, it is the transmitted multiplied by the remaining ray energy (e.g., Malinka, 2014): Then, reflected and transmitted scattering angles are added to their respective bins weighted by the $R$ and $T$ computed from eqs 6 and 7, respectively.

$$W_{\Theta_i} = \begin{cases} R_0 & i = 0 \\ T_0 T_i & i = 1 \\ T_0 \left( \prod_{n=1}^{i-1} R_n e^{-\kappa_\lambda s_n} \right) T_i & i > 1 \end{cases},$$

where $s_n$ is the distance traveled within the particle between the boundary intersections $n - 1$ and $n$. For visible wavelengths, the impact of absorption on the phase function is negligible, however for wavelengths exceeding 1000 nm, it becomes more important. The

At the end of the ray-tracing model, the resulting distribution of energy is converted to a phase function defined relative to the ray total energy initially incident upon the scattering particle rendered snow sample following Grundy et al. (2000):

$$p(cos\cos\Theta_j) = \frac{4\pi N_j}{N sin\Theta_j d\Theta} \frac{4\pi N_j}{N \sin\Theta_j d\Theta}, \tag{11}$$

where $N$ is the total photon energy and $N_j$ is the total photon energy directed into bin $j$.

In practice, while a majority of photons require only a few collisions to reach the 0.1 % energy threshold, we cap the number of internal collisions to a maximum of 10 to limit both computation time and the accumulation of error caused by imperfect 3D particle representations. To evaluate this method, we use it to estimate the phase function of a collection of idealized crystal habits, including spheres, hexagonal plates, and columns with a size parameter of 1000 In this study, the number of bins used to represent the phase function is 180. Accordingly, $d\Theta = 1°$. To illustrate the procedure for generating the optical properties, we show the curve fit for $\gamma_{ext}$, $F_{ice}$, and $p(\cos\Theta)$ for a rendered $\mu$CT sample of snow collected in the field (Fig. 2). We find that these phase functions are in good agreement with Mie Theory for spheres, and with phase functions reported for other shapes presented in previous studies focused on the scattering properties of spherical, idealized, and irregular snow crystal shapes (Iaquinta et al., 1995; Macke et al., 1996; Yang and Liou, 1996; Grundy et al., 2000; Malinka, 2014; Ishimoto et al., 2018). 1).

Schematic illustration of the photon-tracking method used to determine the scattering phase function for a grain with an arbitrary shape.

Phase functions for idealized snow particles following equations ?? and 11 for incident radiation at $\lambda$=900nm. The size parameter ($kL$) for each particle is set to 1000. Note that for the rendered grain, the approximate grain diameter yielded a size parameter of approximately 1400. 500,000 photons were used to generate the phase function. AR is the axis ratio between the long "c" and short "a" axes of the hexagonal column.

## 2.2 1D plane-parallel photon-tracking Model model

Once the required optical properties of the snow sample are determined by launching photons through $\mu$CT sample volumes, a 1D photon-tracking the plane-parallel model is used to simulate snow spectral albedo, transmissivity transmittance, and Bidi-
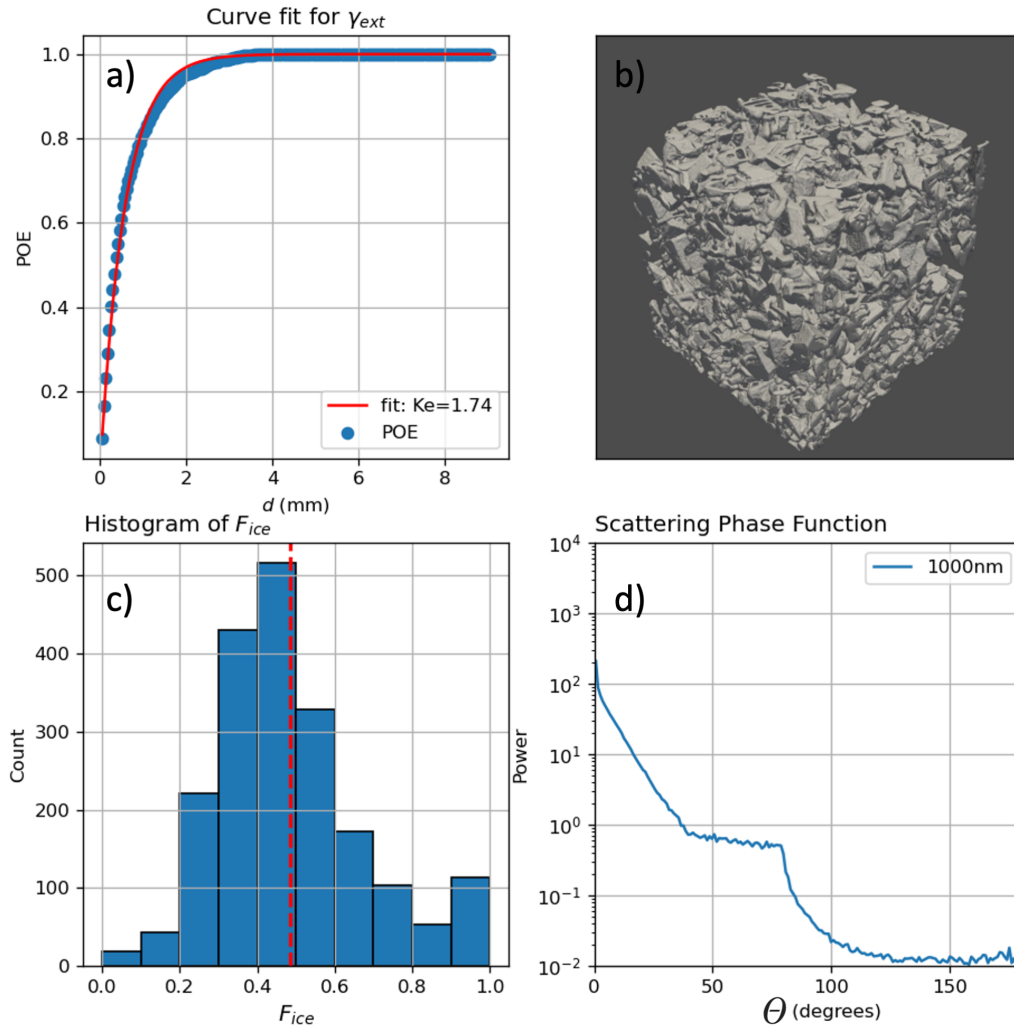
**Figure 1.** Top left: Probability of extinction and curve fit following eq. 3. Top right: 3D rendering a snow sample. Bottom Left: Histogram of $F_{ice}$. Bottom Right: Scattering phase function.

rectional Reflectance Distribution Function (BRDF). The 1D model is used in place of the explicit photon-tracking model
described by Kaempfer et al. (2007) in order to allow for the computationally feasible simulation of spectral albedo and
~~transmissivity~~ transmittance for snow covers with depths exceeding 1 cm with sufficient grain resolution. Additionally, it is
used to avoid complications associated with lateral boundary treatment and stitching multiple $\mu$CT scans together into a single
coherent snow lattice. ~~Our~~ The 1D model ~~is based largely on Jacques (2010), which describes a semi-random 1D multi-layer
Monte Carlo photon-tracking approach for application in the field of biomedical imaging~~used here is largely based on the
framework presented in Jacques (2010) and is similar to the model described in Picard et al. (2016). In this ~~framework~~model,

discrete, plane-parallel, snow layers with optical properties constant throughout each layer are first prescribed. Then a photon packet is initialized at some starting position ($X_0$) with cartesian components of ($x_0$, $y_0$, $z_0$) and an initial energy of unity ($E = 1$). An initial unit direction vector ($V_0$) for the photon is given in cartesian coordinates as:

$$V_0 = \left[ \sin\theta\cos(\phi), \sin(\theta)\sin(\phi), -\cos\theta \right], \tag{12}$$

where $\theta$ is the solar zenith angle, and $\phi$ is the azimuth angle clockwise from $x$. This initial direction can be prescribed randomly (i.e., diffuse radiation), or at any specified zenith/azimuth angle (i.e., direct radiation), or as a mixture of both diffuse and direct radiation.

Once the initial position is set, the photon is launched into the medium, and travels a distance $s$ before experiencing a scattering event. $s$ is computed statistically using the Beer-Lambert law and the medium extinction coefficient (Jacques, 2010):

$$s = -\frac{ln\zeta}{\gamma_{ext}}, \tag{13}$$

where $\zeta$ is a random uniform number between 0 and 1. The new position in the medium is:

$$X = X_0 + sV_0 \tag{14}$$

At the scattering event, the photon packet is given a new direction unit vector according to the scattering phase function. Because this framework treats the scattering phase function as a probability distribution function (PDF), the scattering angle $\Theta$ is determined by choosing a random sample from $p(\cos\Theta)$ PDF:

$$P(\cos\Theta) = \frac{p(\cos\Theta)d\Omega}{4\pi}, \tag{15}$$

where $P$ is the probability of light being scattered into a cone with solid angle $d\Omega$ in the direction $\Theta$ from the incident radiation given the phase function.

Then the new direction vector is determined from $\Theta$ (Jacques, 2010):

$$
\begin{aligned}
\mu_x &= \frac{\sin\Theta\left(\mu_{x_0}\mu_{z_0}\cos\phi - \mu_{y_0}\sin\phi\right)}{\sqrt{1-\mu_{z_0}^2}} + \mu_{x_0}\cos\Theta \\
\mu_y &= \frac{\sin\Theta\left(\mu_{y_0}\mu_{z_0}\cos\phi - \mu_{x_0}\sin\phi\right)}{\sqrt{1-\mu_{z_0}^2}} + \mu_{y_0}\cos\Theta, \\
\mu_z &= -\sqrt{1-\mu_{z_0}^2}\sin\Theta\cos\phi + \mu_{z_0}\cos\Theta
\end{aligned}
\tag{16}
$$

where $\phi$ is given as a uniform random number between 0 and $2\pi$, the 0 subscript represents the incident direction, and $\mu_x$, $\mu_y$, and $\mu_z$ make up the components of the unit direction vector.

Photon energy is depleted over distance $s$ according to the ice absorption coefficient and $F_{ice}$ as determined from the $\mu$CT data instead of using a medium absorption coefficient:

$$E = E_0 \left( e^{-\kappa_\lambda s F_{ice}} \right), \tag{17}$$

where $E$ is the new photon energy, and $E_0$ is the incident photon energy.

To achieve statistical energy conservation, a "Russian Roulette" function is used to determine whether or not to fully absorb (i.e., kill) the photon packet once its energy falls below a prescribed threshold (Iwabuchi, 2006; Jacques, 2010). This is given as:

$$E = \begin{cases} mE & \zeta \le 1/m \\ 0 & \zeta > 1/m \end{cases}, \tag{18}$$

where $\zeta$ is a random number between 0 and 1, and $m$ is a prescribed constant on the order of 1-10. In essence, the Russian Roulette technique achieves energy conservation by proportionally compensating for the energy removed from the model when photons are killed. By treating absorption continuously rather than probabilistically, the number of photons required to attain a robust solution is significantly reduced, and further ensures ~~that the model cannot get stuck in an infinite loop~~stable model integration.

If the $z$ position of a photon-packet is above the top of the snow surface (i.e., it has exited the top of the snowpack), the remaining energy within the packet is added to the total reflected energy and the photon is eliminated. In an open lower-boundary configuration, if a photon-packet $z$ position is less than 0 (i.e., it has exited the bottom of the snowpack) the remaining energy is added to the total transmitted energy, and the photon is eliminated. Alternatively, a lower boundary can be simulated with a specified spectral reflectance such that a portion of the photon energy will be absorbed at the lower boundary, and the remaining energy will be reflected upward. Once all photons have been eliminated from the model, the simulation is complete.

This model is extended to a multilayer configuration ~~,~~ by simply defining unique optical properties corresponding to specified depths throughout the snowpack. When a photon packet travels from one layer to another, its trajectory and energy depletion are determined by the optical properties of the new layer.

The basic premise of this model is illustrated in figure ~~3~~2, which traces the position and energy of two photons on a 2D plane as they travel throughout an idealized two-layer 20 cm deep snowpack~~10 cm deep~~.

## 2.3 Directional Conic Reflectance Function

The reflectance of a surface is often described using the concept of a BRDF (e.g., Stamnes and Stamnes, 2016). ~~This concept essentially represents a PDF of reflected direction of~~ The BRDF represents the directional PDF of reflectance for a ray of light impacting the surface from a ~~given incident direction, and is used to simplify the complex reflectance properties of a rough surface (e. g., shading and multiple reflections).~~ specified incident direction. To estimate the BRDF from this model, we follow the methods described in Kaempfer et al. (2007)~~. In this framework, the BRDF for specified incident zenith and azimuth directions is approximated~~, which approximates the BRDF using the Directional Conic Reflectance Function~~(DCRF ), which~~
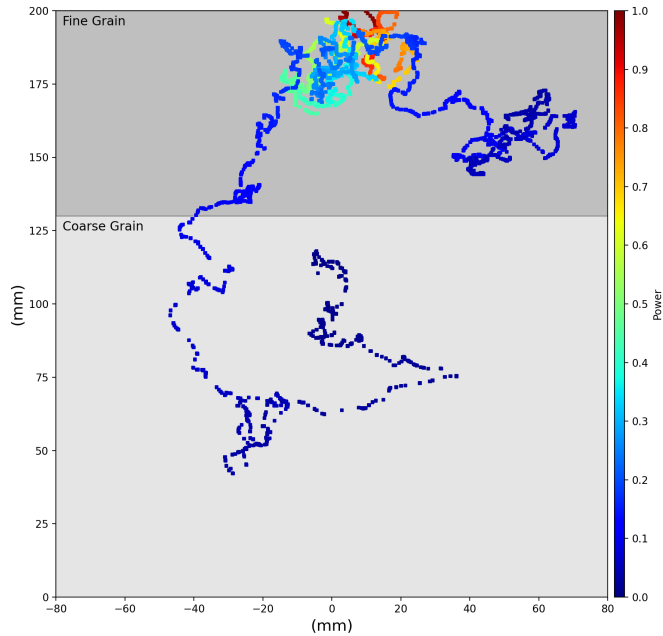
**Figure 2.** x/z cross section of two photons within a multi-layered snowpack ~~10~~ 20 cm deep. The color scale indicates the fractional energy of the photon packet. The ~~gray markers aid in showing~~ background shading indicates the ~~different snow~~ layers ~~. Note that only one photon exits the top~~ of the snowpack~~, the other is fully absorbed in the lower layer.~~Note that the markers are provided as a visual aid, and not ~~representative of the snow particle shape or distribution.~~

~~.~~ The DCRF is a discritized BRDF that computes the energy reflected into a cone in the direction: $\theta_r$,$\phi_r$ subtended by solid angle ~~:~~$d\Omega$:

$$DCRF(\theta_i, \phi_i, \theta_r, \phi_r) = \frac{I_r(\theta_r, \phi_r)}{I_i(\theta_i, \phi_i) cos\theta_i d\Omega} \frac{I_r(\theta_r, \phi_r)}{I_i(\theta_i, \phi_i) \cos\theta_i d\Omega}, \tag{19}$$

where $I$ is the radiative flux, and the subscripts $i$, and $r$ correspond to the incident and reflected radiation, respectively.

## 2.4 Snow sampling and spectroradiometer measurements in the field

To evaluate the model, we collected snow samples and ~~snow surface spectroradiometer measurements~~ spectral reflectance measurements of the snow surface at Union Village Dam (UVD) in Thetford, Vermont several times throughout the 2020-21 winter. The UVD site is a broad flat clearing surrounded by deciduous forests spanning approximately 40000 m$^2$, and bounded on the southern end by the Ompompanoosuc River. During each data collection, a snow pit was excavated and standard snow characteristics, such as snow depth, density, and grain size were measured manually. Several snow samples were carefully extracted at several depths spanning the height of the snow cover in columns adjacent to the snow pit sidewalls in cylindrical

300 containers 7 cm high x 1.9 cm in diameter~~(Fig. 4).~~, with a 1-2 cm overlap in the depth of each sample. Three replicate samples, spaced laterally < 10 cm from one another, at each depth were collected. The specific samples used in this analysis were taken from the surface, 0-7 cm, in the case of the fine grain sample, and from 14-19 cm depth in the case of the coarse grain sample. These samples were transported in a hard, plastic cooler for 10 miles from the UVD site to the Cold Regions Research and Engineering Laboratory (CRREL). ~~At CRREL they were stored in a -20C cold room prior to micro-CT analysis~~The fine grain

305 sample was imaged 18 days after snow sampling, while the coarse grain sample was imaged 53 days after snow sampling. All samples were stored at -30 °C to limit metamorphic change in the intervening timeframe. These samples were not casted (i.e. not preserved using a pore-filler).

~~Photograph showing snow sample collection for μCT analysis.~~

~~Spectral reflectance and transmissivity~~ Spectral reflectance data were collected using a Malvern Panalytical ASD FieldSpec

310 4 Hi-Res: High Resolution Spectroradiometer. The FieldSpec 4 has a spectral range of 350-2500 nm and a spectral resolution of 3 nm in the visible and 10 nm in the SWIR. The data collection was performed within 1.5 hours of solar noon in order to limit high zenith angle impacts. The FieldSpec 4 requires optimization, which adjusts and improves the detector sensitivities for the probe and light source currently in use. An optimization was conducted prior to the start of data collection and any time lighting conditions changed in order to ensure accurate reflectance readings. Data collections were taken 2.5 to 3 feet

315 above the snow surface at nadir using a 5 degree field of view optic lens, resulting in a measurement footprint diameter of approximately 6 cm. The collection strategy employed included taking a white reference reading from a pure reflective panel and five readings at different locations on the target surface; the mean of the five readings was used as the reflectance value for that specific location.

In this paper, we focus specifically on data collected on 12 February, 2021 as this day had the most stable ambient lighting

320 conditions and resulted in the majority of our snow and reflectance measurements. At the time of the measurements the sky was covered with a high optically thick overcast, and as a result the ambient lighting conditions were generally diffuse. The snow was dry and approximately 34 cm deep, and was roughly characterized as a layer of relatively fresh snow approximately 10 cm deep overlying a layer comprised of larger mixed refrozen snow grain clusters and facets, separated by a 1 cm thick ice crust. We performed an initial evaluation of the model against measurements to focus on the effect of shallow snow on the

325 spectral albedo.

## 2.5 ~~μCT sampling and Mesh Generation~~

To measure the effects of a shallow snowpack, a 16"x16" aluminum panel painted black was inserted horizontally into the snowpack through the snow pit sidewall at three depths (10 cm, 4.5 cm, and 2.5 cm) with care as not to damage the smooth snow surface (e.g., Fig. 3). This panel was strongly absorptive in the visible and NIR spectrum with a constant reflectance of

330 approximately 4 % throughout the entire 350 - 2500 nm range. Since there was no appreciable difference between the measured spectral albedo of the virgin snow (i.e., no inserted panel) and the panel inserted at 10 cm, we limit our analysis to the 4.5 and 2.5 cm panel depths.

**Figure 3.** Photograph of the black aluminum panel inserted into the snow pit sidewall approximately 2.5 cm from the surface.

## 2.5 μCT sampling and Mesh Generation

These snow samples were characterized at the microscale with a cold-hardened Bruker Skyscan 1173 μCT scanner housed in a -10 °C cold room equipped with a Hamamatsu 130/300 tungsten X-ray source, which produces a fixed conical, polychromatic beam with a spot size of <5 μm and a flat panel sensor camera detector. Each sample was scanned with 38 kV X-rays at 196 mA and a nominal resolution of approximately 20 μm as the sample was rotated 180° in 0.6° steps with an exposure time of 300-350 ms. Based on estimates of the minimum grain size from manual field measurements, the resolution of the μCT, at 20 μm, is roughly on the order of 10 times the linear size of the minimum grain size we were imaging. We used the commonly employed Nyquist sampling criterion, which requires a minimum of 2.3 pixels per linear feature, to determine that the resolution was sufficient for the grain sizes we sampled. X-rays were detected using a 5 Mp (2240 x 2240) flat panel sensor utilizing 2 x 2 binning, and projection radiographs were averaged over four frames. The resulting 1120 x 1120 pixel radiographs were then reconstructed into 2D gray-scale horizontal slices using NRecon software (Bruker), which utilizes a modified Feldkamp cone-beam algorithm to produce a vertical stack of gray-scale cross-section images. Image reconstruction processing included

345    sample-specific post alignment, Gaussian smoothing using a kernel size of 2 to reduce noise, sample-specific ring artifact correction of dead pixels, beam hardening correction, and X-ray source thermal drift correction. A cylindrical volume of interest with a diameter of 1.6 cm was selected from the scanned samples in order to eliminate edge effects caused by the sampling process.

    Resulting grayscale images are segmented into two phases: air (lowest ~~x-ray~~ X-ray absorption), and snow (highest ~~x-ray~~

350    X-ray absorption). Segmenting thresholds for each phase are determined by finding the local minimum between peaks on the histogram showing all grayscale values, and using that value as a global threshold for each scanned sample. The resulting binarized data are despeckled so that any objects less than 2 pixels in diameter were removed.

    The final binarized images are then used to construct 3D representations of dry snow samples for input into the RTM. This is accomplished through the use of open-source image processing and 3D visualization software packages accessed through

355    Python (Schroeder et al., 2004; Van der Walt et al., 2014; Sullivan and Kaszynski, 2019). ~~From the binarized images, the first step is to detect and mark individual snow grains. This can prove difficult as the grains are sintered together and their definition can be subjective. However, there is a wide body of literature on grain segmentation methods (e.g., Mangan and Whitaker, 1999; Wang et al. Here, we use a common grain segmentation threshold technique called watershed segmentation due to its relatively easy implementation, computational efficiency, and accuracy. To apply this method we first combine a stack of binarized images~~

360    ~~and construct a 3D point cloud sub sample of approximately 800 mm$^3$ ($\approx$ 450$^3$ voxels) and calculate the Euclidean distance transform of the point cloud. Markers are then generated for the local maxima of the distance to the background. The watershed algorithm treats pixel values as a local topography and floods basins from the markers until basins attributed to different markers meet on watershed lines, which tend to occur along physical grain boundaries. From this, individual grains are extracted from the sample.~~

365    To build a full sample mesh, ~~the grains are processed on an individual basis and then combined together to create the full mesh. To process each individual grain,~~ a contour-based surface reconstruction process was developed to generate ~~grain~~ snow surfaces from the voxels that make up the ~~grain~~snow sample. This method uses a subset of the binary sample array~~that contains the target grain~~, including both snow and adjacent air voxels. The subset array is then refined to increase the resolution. A Gaussian filter is applied to smooth the refined array, diminishing pixelated appearance of the voxelized snow-air interface,

370    producing a smooth level set from which to extract the ~~grain surface(Fig. 5).~~ snow surface. The smoothed level set is then used to define an isosurface at the snow-air boundary, providing control over where the boundary is drawn with respect to the voxels.

    ~~a) Point cloud representation of an example grain. b) surface rendering of the point cloud.~~

    Finally, to extract the isosurface from the 3D voxel array, we apply the Marching Cubes method. ~~In this technique, the input volume is divided into a discrete set of cubes . The algorithm then determineshow the surface intersects with a given cube, based on the classification of the surrounding vertices and calculates an index for the cube by comparing the sample~~ This

375    algorithm iterates through defined cubes (i.e. voxels) and determines, through knowledge of the pixel values at the ~~vertices with the given isosurface value. From these results, it uses a pre-calculated look-up-table of various surface-edge intersections possible with the cube. Finally, the algorithm finds the surface-edge intersection through linear interpolation, resulting in a triangulated mesh. The algorithm "marches" through each cube. The~~ cube vertices, if the isosurface intersects that cube. If
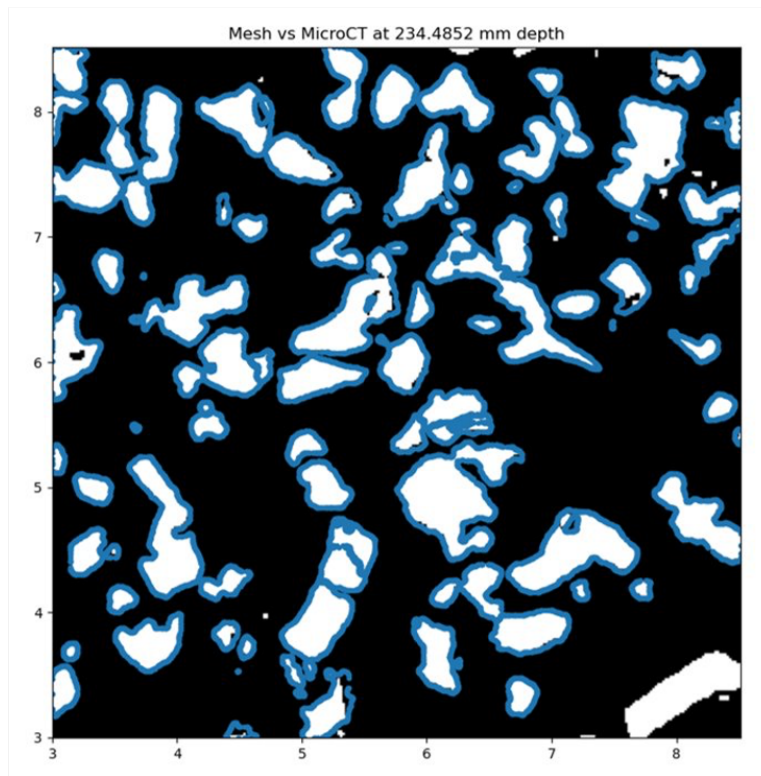
**Figure 4.** 2D Cross-sectional slice of a binarized $\mu$CT scan with corresponding mesh boundaries superimposed shown as the blue lines.

380    so, it creates triangular patches via a lookup table that are eventually connected to form the isosurface boundary. The orig-
inal algorithm presented by Lorensen and Cline (1987) can lead to cracks and over the years has been improved by many
~~(Nielson and Hamann, 1991; Scopigno, 1994; Natarajan, 1994; Chernyaev, 1995; Lewiner et al., 2003)~~(Nielson and Hamann, 1991; Scopi
For this work, we used the adaptation implemented by Lewiner et al. (2003), which improved the algorithm to resolve face and
internal ambiguities, extended the lookup table, and guaranteed correct topology. As a final step, each grain is "repaired" to

385    remove any defects and degenerate elements and ensure a manifold surface according to Attene (2010), and then decimated to
reduce the overall number of triangles that comprise the surface thereby lowering the computational requirements. Overall, this
method appears to accurately characterize the snow within the $\mu$CT sample with computed mesh snow sample densities within
1.5% of snow densities computed from the raw voxels. Figure ~~6~~ 4 shows a 2D cross section comparing ~~grain~~ air/ice boundaries
to the raw pixels of the image and selected example 3D rendered ~~grains are show in Figure 7~~ samples are shown in Figure 5.
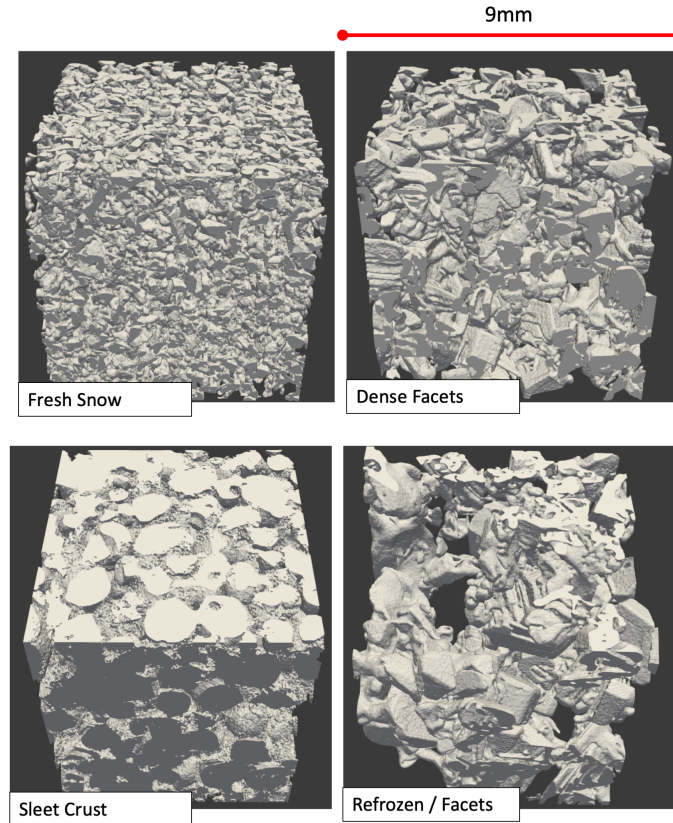
**Figure 5.** Example 3D renderings of ~~selected~~ μCT sample representing different ~~snow grains. These grains represent a variety of snow~~ types~~including fresh snow aggregates (a, c), elongated needles (b), and faceted grain fragments (d,e), and sleet (f).~~

## 3 Results

### 3.1 General Evaluation

An initial evaluation of the model is performed by simulating the spectral albedo for two idealized ~~20~~ 60 cm deep snowpacks with uniform optical properties throughout. For these snowpacks, the optical properties are determined from 3D meshes generated by two characteristically distinct μCT samples. One mesh is representative of fresh, fine-grained snow near the surface, and the other of large facets near the bottom of the snowpack (Fig. ~~8~~6). For each mesh, the total mesh volume is approximately 800 mm$^3$. Additional physical and optical properties of ~~the~~ each mesh are presented in Table 1. For each sample, the spectral albedo is computed for wavelengths between ~~400-1300 nm at 25~~ 400-1600 nm at 20 nm intervals with diffuse incident radiation. This comparison demonstrates that the model capably reproduces ~~some~~ a known behavior of spectral albedo, ~~and specifically, it shows a strong wavelength dependence on snow microstructure that favors the NIR~~ namely the strong sensitivity of NIR albedo to snow microstructure (Fig. ~~9~~7a). The spectral albedo is relatively uniform between the two snowpacks for the spectral
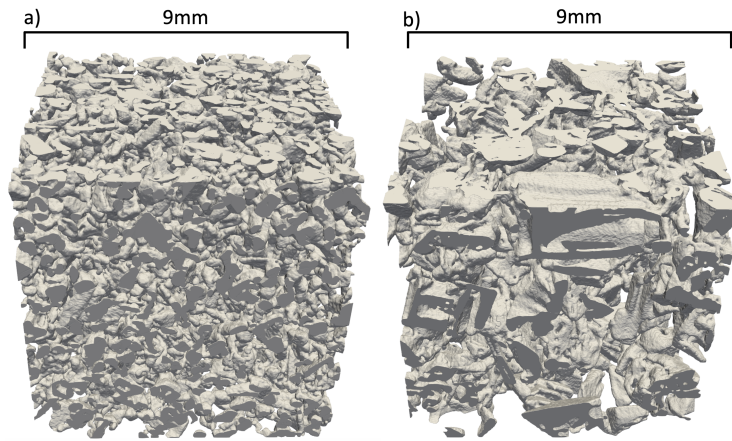
**Figure 6.** 3D renderings of mesh samples used to generate the optical properties for the general evaluation and snow ~~transmissivity~~ transmittance comparisons. a) Fine grain sample, and b) Coarse grain sample.

**Table 1.** Physical and optical properties of the fine grain and coarse grain mesh samples. Note that SSA and $\rho_s$ are computed directly from the $\mu$CT sample.

| Property | Fine Grain | Coarse Grain |
|:---:|:---:|:---:|
| SSA (m$^2$ kg$^{-1}$) | ~~19.29~~ 18.4 | ~~12.85~~ 12.9 |
| $\rho_s$ (kg m$^{-3}$) | ~~263~~ 286.99 | ~~232~~ 282.4 |
| $\gamma_{ext}$ (mm$^{-1}$) | ~~1.86~~ 2.22 | ~~0.99~~ 1.65 |
| $F_{ice}$ | ~~0.44~~ 0.48 | ~~0.41~~ 0.49 |
| $B$ | 1.55 | 1.48 |

range between 400 and 800 nm, and then the albedos diverge, with a more rapid decrease in albedo for the coarser-grained snow.

We then assess the ~~relationship between~~ dependence of simulated spectral albedo ~~and~~ on incident zenith angle for the fine grain snow sample at four different wavelengths to evaluate the model's ability to simulate anisotropy in the surface reflectance (Fig. ~~9~~7b). This analysis shows an exponential increase in albedo at high zenith angles that is most pronounced in the NIR, consistent with ~~observed behavior. This result indicates that the model is capable of simulating surface anisotropy with good fidelity~~the results from previous studies that compare snow albedo and zenith angle (e.g., Li and Zhou, 2003; Kokhanovsky and Zege, 2004). As a related evaluation, the model-simulated DCRF is computed as a function of zenith angle (Fig. ~~10~~8). This analysis reveals that the reflectance is mostly isotropic for zenith angles less than approximately 55° at which point the surface becomes increasingly forward scattering, consistent with previous observational and modeling studies ~~(Kaempfer et al., 2007; ?; Xiong et al., 2015; Jiao et a~~
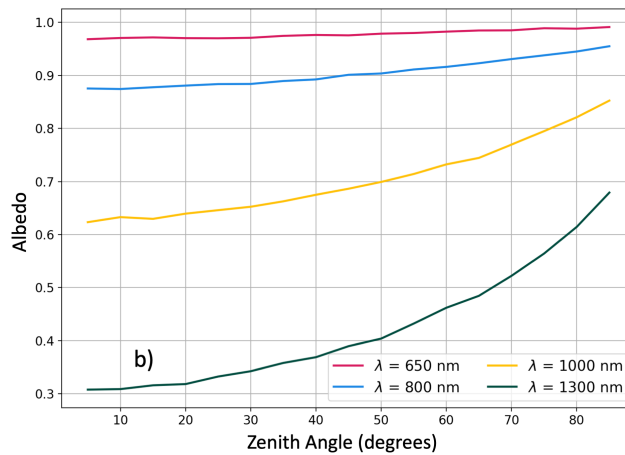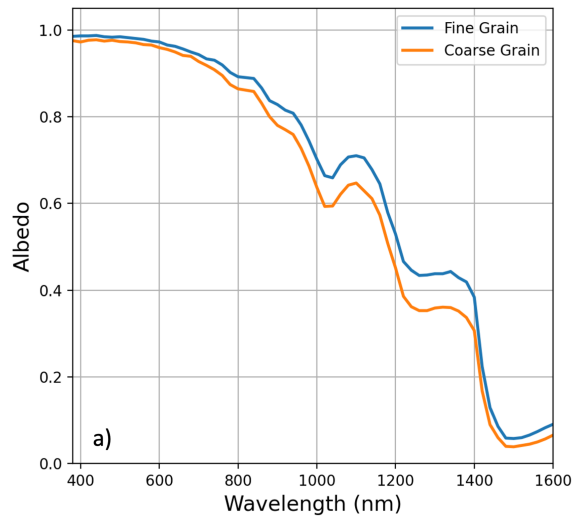
**Figure 7.** a) Simulated spectral albedo for fine grain and coarse grain snow samples for 100% diffuse radiation. b) Simulated spectral albedo as a function of incident zenith angle for selected wavelengths. Note that both simulations were run with 25000 photons for a snow depth of 60 cm.

Finally, we use the model to provide an initial assessment of the impacts of snow microstructure on simulated spectral transmissivitytransmittance at specified depths within a homogenous snowpack. To accomplish this, the optical properties of the $\mu$CT samples in Fig. 8 6 are used to simulate and compare the spectral transmissivity transmittance at varying depths (Fig. 119). The transmissivity transmittance is highest at the short, non-absorptive, wavelengths and gradually decreases throughout the NIR, broadly matching quantitative snow transmissivity transmittance results reported in Perovich (2007) and Libois et al. (2013). The depth of the 5% transmissivity transmittance contour for the fine-grain fine grain snow sample is approximately 2.5 6 cm for the visible, and decreases to approximately 1.5 2 cm for the NIR (Fig. 119a), indicating that the fine-grain snow optical thickness fine grain snow penetration length is on the order of only a few centimeters. In contrast, the transmissivity

$\theta = 5.0°$  $\theta = 10.0°$  $\theta = 15.0°$  $\theta = 20.0°$
$\theta = 25.0°$  $\theta = 30.0°$  $\theta = 35.0°$  $\theta = 40.0°$
$\theta = 45.0°$  $\theta = 50.0°$  $\theta = 55.0°$  $\theta = 60.0°$
$\theta = 65.0°$  $\theta = 70.0°$  $\theta = 75.0°$  $\theta = 80.0°$
$\theta = 89.0°$

**Incident Radiation**
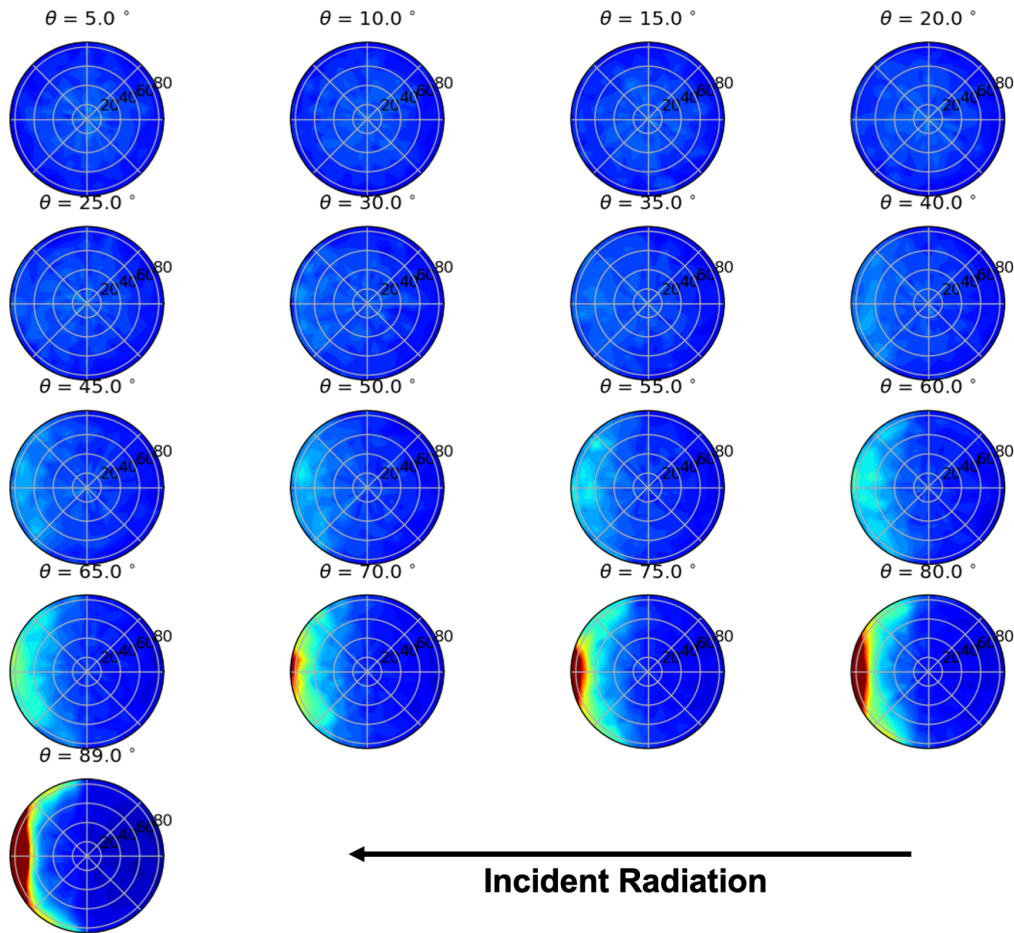
**Figure 8.** Polar plots of DCRF at 1000 nm for incident zenith angles ranging from 5 - 89°. Reflected azimuthal direction is on the theta axis, and reflected zenith angle ~~if~~ is on the $r$ axis. Color scale ranges from 0-1.5.

transmittance for the coarse grain snow is ~~increased~~ greater near the surface, and the depth of the 5 % contour ~~increases to 7.5~~ correspondingly increases to 12.5 cm for the visible and ~~3~~ 5 cm for the NIR (Fig. ~~11~~9b).

## 3.2 Evaluation against UVD Data

~~An initial evaluation of this framework is performed against spectoradiometer data collected on 12 February 2021 at the UVD study site. At the time of the measurements the sky was covered with a high optically thick overcast, and as a result the ambient lighting conditions were generally diffuse. The snow was dry and approximately 34 cm deep, and was roughly characterized as a layer of relatively fresh snow approximately 10 cm deep overlying a layer comprised of larger mixed refrozen snow grain clusters and facets, separated by a 1 cm thick ice crust. To simulate~~ To evaluate the model's ability to simulate the effect of
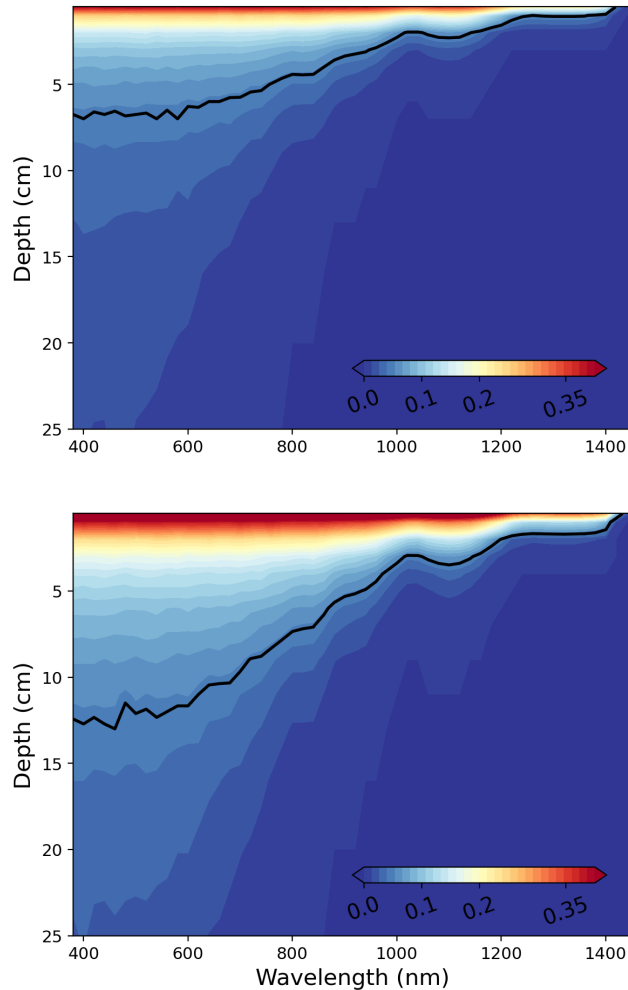
**Figure 9.** ~~a)~~ Simulated ~~transmissivity~~ transmittance of a) the fine grain snow~~sample contoured as a function of depth~~ , and ~~wavelength.~~ b) ~~Transmissivity difference between~~ the coarse grain ~~and fine grain~~ samples contoured as a function of ~~wavelength and~~ depth and wavelength. ~~The~~ Solid black lines mark the depth of the 5 % ~~transmissivity~~ transmittance contour~~is plotted for the fine grain (black) and coarse grain (red) samples~~.

the ~~effects of a shallow snowpack, an aluminum panel painted black with paint that had a lower than 5 % reflectance at all visible and NIR wavelengths was inserted into the snowpack through the snow pit sidewall at three depths (10 cm, 4.75 cm, and 2.5 cm) within the snow with care as not to damage the smooth snow surface (e.g., Fig. 12). Since there was no appreciable~~

430 ~~difference between the measured spectral albedo of the virgin snow(i.e., no inserted panel) and the panel inserted at 10 cm, we limit our analysis to the 4.75 and 2.5 cm panel depths.~~

**Table 2.** Physical and simulated optical properties of the top 8 cm of snow measured at the UVD site on 12 February, 2021. SSA and $\rho_s$ are computed directly from the $\mu$CT sample. Note that the depths correspond to the RTM model depths for the virgin snow calculation.

| depth [cm] | SSA (m$^2$ kg$^{-1}$) | $\rho_s$ (kg m$^{-3}$) | $\gamma_{ext}$ (mm$^{-1}$) | $F_{ice}$ | $B$ |
|---|---|---|---|---|---|
| 1 (32-34) | 26.1 | 147 | 1.41 | 0.32 | 1.89 |
| 2 (30-32) | 27.2 | 178 | 1.85 | 0.34 | 1.64 |
| 3 (28-30) | 21.1 | 250 | 2.30 | 0.44 | 1.52 |
| 4 (0-28) | 18.4 | 287 | 2.22 | 0.48 | 1.55 |

The underlying surface on snow spectral albedo for shallow snow, optical properties used in the plane-parallel model were determined from four approximately 800 mm$^3$ $\mu$CT samples, with each sample representing a 2 cm thick layer within the top 8 cm of the snowpack. The RTM is then configured with 4 layers according to these optical properties (given in Table 2). The top three layers are each 2 cm thick, and the bottom layer is 28 cm thick, such that the entire snow depth amounted to 34 cm. We chose this configuration in accordance with the hypothesis that the snow microstructure below 8 cm had little impact on the measured surface spectral albedo. To simulate the panels, the snowpack depth is modified to be 4.75 and 2.5 cm deep with a lower boundary consistent with the spectral reflectively of the black panel (Table 2).

There is generally good agreement between the observations and the model (Fig. 10) and in particular, the model accurately simulates the impact of the inserted panel on the surface albedo for wavelengths shorter than 1000 nm for both the 4.5 and 2.5 cm depths. The model spectral albedo decreases more rapidly with wavelength in the 800 - 1000 nm region, particularly for the virgin snow sample. This leads to a slight underestimate in albedo in the NIR range for wavelengths shorter than 1400 nm, beyond which there is a slight overestimate. However, for wavelengths longer than 1400 nm, differences between the model and observations may be due to the limitation of the geometric optics approximation as the approximate particle size parameter is $< 1000$ for $\lambda > 1400$ nm.

### 3.3 Snow optical and physical properties

A final analysis is performed to determine how strongly The model can also be leveraged to assess the relationship between common snow physical properties relate to and the simulated optical properties from this framework. To demonstrate this, we compare snow specific surface area (SSA) and snow sample density ($\rho_s$) to $\gamma_{ext}$ and $F_{ice}$. This analysis is performed by generating optical properties from several $\mu$CT sample volumes collected on different dates
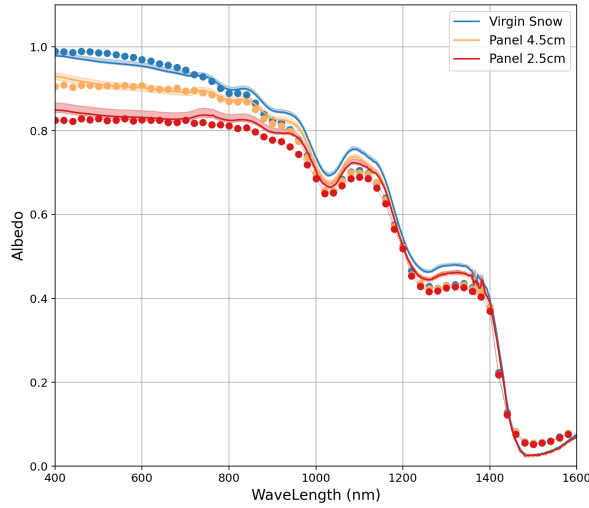
**Figure 10.** Simulated and observed spectral albedo ~~at UVD~~ for three different snow depths. ~~Solid~~ The solid lines indicate observations and dotted lines indicate simulations. The shading around the observations indicates the inter-quartile range of the measurements computed from the five snow and two reference scans collected during each measurement, providing an assessment of measurement uncertainty. ~~Mean~~ The mean RMSE of the simulated albedo compared to measurement-derived albedo over ~~400-1600nm~~ 400-1600 nm is equal to ~~0.06~~ 0.04

~~and for various~~ and locations during the 2020-2021 winter season, spanning a wide range of snow types. Note that each $\mu$CT sample is approximately 800 mm$^3$ and the sample SSA and $\rho_s$ are determined from the $\mu$CT 3D rendering.

This analysis reveals that $F_{ice}$ has a very robust relationship with snow density (Fig. ~~??~~11a) described by the linear fit:

$$F_{ice} = \underline{0.00074}0.0008\rho_s + \underline{0.25}0.22, \tag{20}$$

460     with $r^2 = 0.81$. ~~In contrast, while~~ $r^2 = 0.92$. In Figure 11b, $\gamma_{ext}$ ~~generally seems to increase as a function of SSA, this relationship is not as well constrained as the relationship between $\rho_s$ and $F_{ice}$ (Fig. ??b). Instead, we find that $\gamma_{ext}$ is generally better approximated by a multivariate regression function that includes both SSA and density:~~

$$\gamma_{ext} = 0.077SSA + 0.0028\rho_s - 0.59,$$

~~with $r^2 = 0.26$. Interestingly, this relationship can be improved substantially by removing the ice-crust samples from the~~
465     ~~dataset. This change modifies eq. 20~~ is compared to the product of $\rho_s$ and SSA, to match the analytical formula described in Kokhanovsky and Zege (2004). The results show a clear linear relationship fit to:

$$\gamma_{ext} = 0.085SSA0.092 + 0.00620.4\rho_s - 1.51_sSSA, \tag{21}$$

~~and increases $r^2$ to from 0.25 to 0.79. This relationship dictates that the extinction coefficient increases both as a function of SSA and $\rho_s$, indicating that the highest extinction coefficients will be associated with small, tightly packed snow grains.~~ ~~In contrast, with ice-crusts the extinction coefficient is more strongly related to SSA, and largely independent of $\rho_s$, leading to low extinction coefficients despite very high snow densities, counteracting the relationships described in equations 20,21. Overall, these results suggest that commonly observed physical snow properties can be used to approximate optical properties in conjunction with an appropriate phase function for the medium photon-tracking RTM model for non-crust snow layers~~with $r^2 = 0.73$.

The estimated $B$ parameter is distributed normally around a mean of 1.49, consistent with the results reported in Libois et al. (2014). We note that there is no significant relationship between $B$ and snow grain form or size, however there is a general tendency for $B$ to be highest for samples with higher SSA and smaller rounded grains consistent with Kokhanovsky and Zege (2004) and Libois et al. (2014).

To further assess how these two specific snow optical properties, $\gamma_{ext}$ and $F_{ice}$, affect the greater simulated spectral ~~transmissivity~~transmittance, we perform a sensitivity analysis by comparing the 5% ~~transmissivity~~ transmittance contour depth for three fractional ice paths: ~~0.30, 0.46, 0.69~~ 0.31, 0.47, 0.75 at two fixed $\gamma_{ext}$ values: ~~2.34, 0.81~~2.65, 0.91 mm$^{-1}$. The two $\gamma_{ext}$ values correspond to the max, min values found in the previous analysis and presented in Fig. ~~??~~12b. The three $F_{ice}$ values correspond to the max, min, and mean values (Fig. ~~??~~12a). We compare the influence of $F_{ice}$ at both the max and min $\gamma_{ext}$ values, since we anticipate the strength of its influence will vary according to $\gamma_{ext}$. ~~While we pair the maximum $\gamma_{ext}$ with the $F_{ice}$, we~~ We note that high values of $\gamma_{ext}$ are more likely to coincide with high values of $F_{ice}$ due to the shared dependence of these variables on snow density in most snowpacks.

The results of this analysis indicate that both $\gamma_{ext}$ ~~has a much larger impact on snow transmissivity than $F_{ice}$. This is unsurprising due to the highly scattering nature of snow. In particular the snow medium is much more transmissive at the minimum $\gamma_{ext}$ value with the 5 % transmissivity contours exceeding 7 cm in the visible and~~ and $F_{ice}$ impact snow transmittance in accordance with relationships discussed in Libois et al. (2013). Specifically, the factor of 3 ~~cm in the NIR. This is in contrast to the transmissivity of the maximum extinction coefficient, which never exceeds 4 cm of depth (Fig. ??).~~ decrease in the extinction coefficient corresponds to a factor of 3 increase in depth of the 5 % transmittance contour, consistent with a linear relationship between $\gamma_{ext}$ and penetration depth ($L$). Additionally, the simulated factor-increase in penetration depth is approximately the square root of the factor increase in $F_{ice}$~~can either amplify or dampen the effect of $\gamma_{ext}$ in the NIR, with~~ ~~lower values of $F_{ice}$ leading to in increase in transmissivity at a given depth compared to high values of $F_{ice}$,~~ for $\lambda > 600$ nm, consistent with the $L \approx \sqrt{B * \kappa_{abs}}$ presented in Libois et al. (2013).

## 4 Discussion
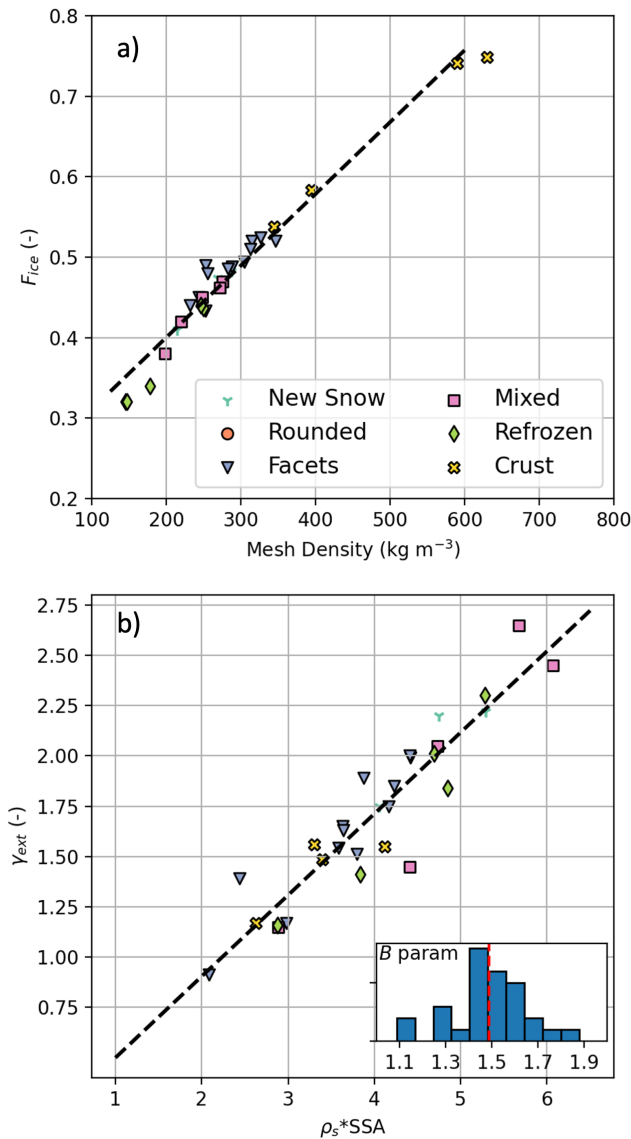
**Figure 11.** Optical properties for $\lambda$=~~900nm~~ 1000 nm computed from $\mu$CT photon-tracking compared against sample physical properties. a) $F_{ice}$ vs. $\rho_s$ and b) $\gamma_{ext}$ vs. ~~SSA~~ SSA*$\rho_s$. Linear regression lines are shown in black dashed lines. ~~Note that the regression line plotted on (b) is a single-parameter regression line for illustrative purposes,~~ Marker shapes and ~~not~~ colors are indicative of ~~the multi-parameter regression discussed in the text. Snow~~ observed grain forms ~~were~~ determined through visual assessment during snow pit analysis. Note that in panel (b) a histogram of the estimated B parameters for all of the $\mu$CT samples is shown, inset. $B_{mean} = 1.49$ is shown as the vertical red line.

~~One key objective of this work is to expand beyond determining snow optical properties from a specified distribution of grains with idealized shapes, and instead represent snow as an organized structure in determining them. One snow type where this~~
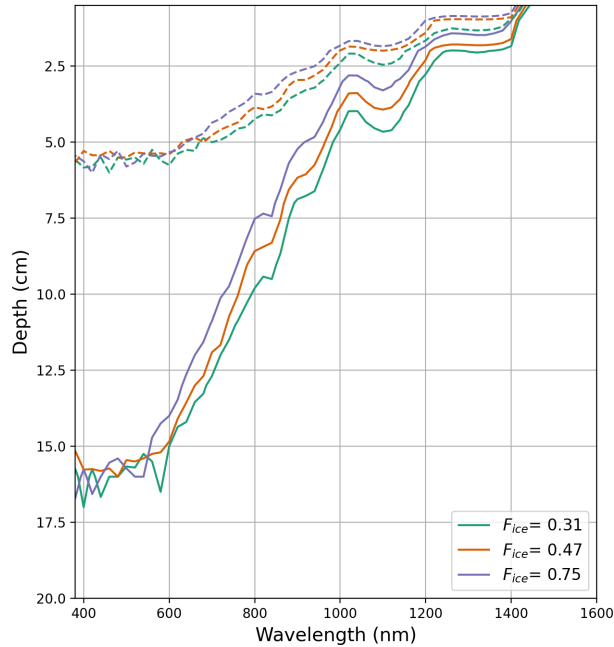
**Figure 12.** Depth of simulated 5% ~~transmissivity~~ transmittance contour as as a function of wavelength for varying $F_{ice}$ at two extinction coefficient: ~~$\gamma_{ext} = 0.81$~~ $\gamma_{ext} = 0.91$ (Solid lines) and ~~$\gamma_{ext} = 2.34$~~ $\gamma_{ext} = 2.65$ (Dashed lines).

500 ~~approach may be particularly advantageous is in understanding the optical properties of snow crust layers, which do not fit easily into the collection of particles or air bubbles approximation. This is supported by our finding that~~

Overall, this framework shows promise as a research tool for better understanding visible and NIR snow radiative transfer through snowpacks with irregularly shaped and arranged grains. However, there are numerous uncertainties in this framework that should be addressed in future work to better understand its capabilities and limitations.

505 For example, foundational work on light scattering in a collection of weakly absorbing particles indicates that, ignoring diffraction, $\gamma_{ext}$ is given as ~~$\gamma_{ext}$ is very well approximated with a multivariate regression of SSA and $\rho_s$ for all observed snowtypes except for crusts, which exhibited the highest snow densities and~~ $= \rho_s SSA/4$ (e.g., Hulst and van de Hulst, 1957; Kokhanovsky In this work, we find $\gamma_{ext}$ to be related to $\rho_s SSA$ by a factor of approximately 2/5, rather than 1/4 (eq. 21). We speculate that this is because the method for determining $\gamma_{ext}$ described in Xiong et al. (2015) and extended into three-dimensions here,

510 initializes photons randomly throughout the sample, which relaxes the assumptions regarding particle projected area implicit within the $\gamma_{ext} = \rho_s SSA/4$ relationship. To explore this, we performed a test in which we computed $\gamma_{ext}$ for artificial snow samples comprised of rendered spheres generated with specified $\rho_s$ and SSA (not shown). The results of this test were in broad agreement with the ~~lowest extinction coefficients and SSAs. Another snow type this approach may be well suited for is highly~~
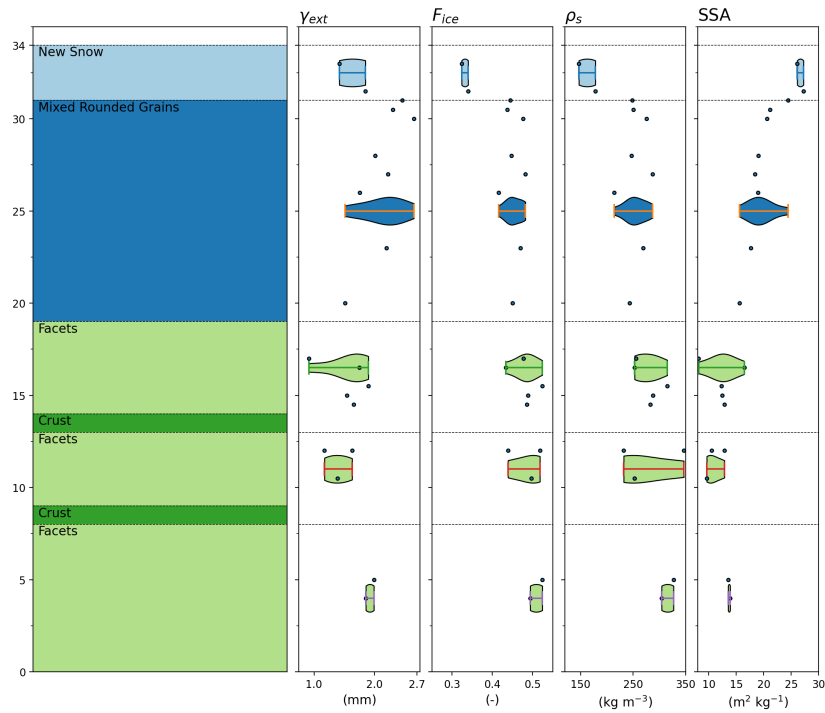
**Figure 13.** Snow pit stratigraphy (right) compared against $\gamma_{ext}$, $F_{ice}$, $\rho_s$, and SSA. Violin plots show estimated probability distributions for each observer-identified snow layer according to the samples collected with the layer.

~~aged snow that has metamorphosed into a collection of large irregularly shaped grain clusters and pore spaces.~~ 2/5 factor, and
more similar to results presented in Xiong et al. (2015), supporting this hypothesis. However, more work should be performed in the future to better understand this discrepancy.

One possible significant source of uncertainty in this framework is the assumption that the optical properties computed from volume $\mu$CT samples on the order of 1 cm$^3$ are homogeneous laterally, and can be extrapolated to characterize representative layer depths. To elucidate upon this uncertainty, we compare the optical and physical properties of the 20 rendered $\mu$CT samples collected at UVD on 12 February 2021 to the observed snow pit stratigraphy (Fig. 13).

Here we show that the top layer of the snowpack has more homogeneous physical and optical properties than the buried layers. In particular there is substantial variability in $\gamma_{ext}$ and $F_{ice}$ within the rounded grains and the upper-most facet layers. Further investigation into this variability in the facet layer spanning the 14-18 cm layer reveals that this variability is caused largely by the fact that some $\mu$CT samples within this layer contained unusually large pore spaces, which caused lower SSA and $\gamma_{ext}$ values. We suspect that this variability has limited impacts on the simulated spectral albedo for the simulations focused on shallow snow, since the top most snow layer is relatively homogeneous. However, this variability is likely to have more significant impacts for simulations focused on older snowpacks with larger and less uniformly distributed snow grains.

~~While ideally~~Similar to several previous studies (Carmagnola et al., 2013; Dumont et al., 2021), we found model discrepancies to be greater in the NIR, underestimating albedo between 800 and 1400 nm, and overestimating above 1400 nm. This could, in part, be due to the observations as the lighting conditions were not ideal. An additional potential source of uncertainty in the model are the ice refractive indices, which we have taken to be constant. For example, Carmagnola et al. (2013) attributed their discrepancies to their choice of ice refractive index, with varying values reported in the literature.

Ideally, the optical properties ~~would~~ used in the model should vary slightly with wavelength ~~due to the impact of absorption on~~ as there are minor spectral variations in $\gamma_{ext}$ and ~~the phase function, we~~ $p(\cos\Theta)$. We chose to leave the optical properties independent of wavelength ~~. This choice is made entirely~~ to reduce the computational burden of running the photon-tracking model for several wavelengths. Cursory sensitivity tests performed to assess the impact of this choice on the optical properties supported the use of wavelength-independent optical properties, as both ~~$p(cos\Theta)$~~ $p(\cos\Theta)$ and $\gamma_{ext}$ exhibited generally a negligible dependence on wavelength for $\lambda > 1400$ ~~. We suspect that this is due to the fact that a ray is much more likely to be scattered at an air/ice boundary than by absorption within the particle (i.e., snow has a high single scattering albedo). This may not be the case for all snow types, in particular for the NIR wavelengths within very large grains, and is worthy of future exploration~~nm (not shown), and we anticipate that source of uncertainty is small relative to the sources discussed above.

## 5 Conclusions

In this work we have presented a blended photon-tracking radiative transfer model in an effort to better understand the complicated influence of snowpack microstructure on snow spectral ~~transmissivity~~ transmittance in the geometric optics limit. A ~~foundational~~ primary goal of this modeling approach is to expand upon previous approaches aimed at incorporating 3D renderings of real snow microstructure into radiative transfer models for snowpacks of arbitrary depth, while maintaining the Monte Carlo aspects of the model. To accomplish this, existing methods for simulated photon interactions with rendered elements are employed to determine key optical properties of the snow (Grundy et al., 2000; Kaempfer et al., 2007; Xiong et al., 2015).

An evaluation of this framework for consistency with known behavior of spectral snow albedo revealed that this framework can successfully reproduce the dependency of spectral albedo and grain size, as well as the surface anisotropy at high incident zenith angles, found in previous studies. Furthermore, ~~a~~ an initial comparison of the simulated snow albedo against ~~spectroradiometer measurements collected~~ albedo measured in the field over snow with varying depths ~~indicate~~ indicates that the model can simulate the effects of an underlying surface on spectral albedo with ~~high~~ sufficient accuracy.

In comparing two different snow samples, it was revealed that snow microstructure has a large impact on snow ~~transmissivity~~ transmittance in the visible spectrum and near the snow surface, increasing the 5 % ~~transmissivity depth from approximately 4~~ transmittance depth at 400 - 650 nm from approximately 6 cm for a fine grain snow sample to ~~7.5~~ 12.5 cm depth for a coarse grain sample. These values and the ability to further constrain the transmittance depths of shallow snowpacks will allow for improved capabilities for determining the visibility of subnivean hazards. A brief sensitivity analysis of the optical properties revealed that lowering the medium extinction coefficient acted to ~~reduce the albedo and increase transmissivity~~ increase the transmittance depth in the visible bands, while the fractional ice path ($F_{ice}$) impacted the rate at which albedo and ~~transmissivity~~

transmittance decreased as a function of wavelength in the NIR. ~~Accordingly, we anticipate that snowpacks made up of large grains with low fractional ice-paths will be the most transmissive.~~

Overall, while current efforts are focused on using this model to better understand snow ~~transmissivity~~transmittance, it shows promise as a broadly applicable snow RTM that has a strong direct connection to $\mu$CT snow samples. While currently ~~,~~ it is limited to the geometric optics approximation for clean snow and unpolarized radiation, ongoing and anticipated future efforts are aimed at improving the grain segmentation and rendering process, incorporating polarization, parameterizing diffraction, and including light absorbing particulates (LAPs). In particular, recent multiphase image segmentation techniques ~~(e.g., West et al., 2018)~~ (West et al., 2018; Hagenmuller et al., 2019) could be used to better separate snow, air, and LAPs in a $\mu$CT sample allowing for the impact of LAPs to be determined through ray-tracing. Furthermore, because the model operates entirely as a photon-tracking model, it is a natural fit with ~~macro-scale~~ macroscale ray-tracing and therefore could be used to investigate the reflectance of rough snow surfaces such as sun cups or sastrugi.

*Code and data availability.* The mesh generation and RTM code with associated documentation is available in preliminary 'as is' format on Github at (lhttps://github.com/wxted/CRREL-GOSRT.git). Sample data files used to generate figure 9a is available on Github as sample data. Additional limited sample data, including rendered microCT meshes, and spectroradiometer data used for this paper are available upon request.

*Author contributions.* Theodore Letcher performed a majority of the model physics, structural development, and coding, in addition to coordinating the model analysis and manuscript preparation. Julie Parno led research and coding efforts related to the 3D mesh generation and rendering and assisted in general coding, she also coordinated a majority of the fieldwork activity. Zoe Courville provided research support, participated in snow sampling and coordinated $\mu$CT analysis. Lauren Farnsworth performed a large portion of $\mu$CT scans and a majority of the $\mu$CT image post processing and analysis. Jason Olivier participated in fieldwork and provided background on the ASD instrumentation and sampling for the manuscript. Theodore, Julie, and Jason performed the RTM simulations and assisted in code debugging. All authors provided writing support for the manuscript.

*Competing interests.* The authors declare that no competing interests are present

*Acknowledgements.* We wish to acknowledge Dr. Arnold Song from Dartmouth College in Hanover, New Hampshire for providing relevant code examples to facilitate 3D shape rendering. We also wish to thank Taylor Hodgdon from CRREL for providing occasional support and advice on using Python to perform snow grain segmentation and rendering. Finally, we wish to thank Dr. Bert Davis, and Dr. Ned Bair for providing valuable initial feedback on the manuscript. Funding support for this research was provided by the U.S. Army Engineer Research

and Development Center (ERDC) Cold Weather Military Research project. **Place Holder to thank reviewers** Finally, we would like to sincerely thank the reviewers for providing a thorough and engaging review which substantially improved the quality of this manuscript.

## References

Adolph, A. C., Albert, M. R., Lazarcik, J., Dibb, J. E., Amante, J. M., and Price, A.: Dominance of grain size impacts on seasonal snow albedo at open sites in New Hampshire, Journal of Geophysical Research: Atmospheres, 122, 121–139, 2017.

Aoki, T., Aoki, T., Fukabori, M., Hachikubo, A., Tachibana, Y., and Nishio, F.: Effects of snow physical parameters on spectral albedo and bidirectional reflectance of snow surface, Journal of Geophysical Research: Atmospheres, 105, 10 219–10 236, 2000.

Attene, M.: A lightweight approach to repairing digitized polygon meshes, The visual computer, 26, 1393–1406, 2010.

Bair, E. H., Rittger, K., Skiles, S. M., and Dozier, J.: An examination of snow albedo estimates from MODIS and their impact on snow water equivalent reconstruction, Water Resources Research, 55, 7826–7842, 2019.

Bohren, C. F. and Beschta, R. L.: Snowpack albedo and snow density, Cold Regions Science and Technology, 1, 47–50, 1979.

Carmagnola, C., Domine, F., Dumont, M., Wright, P., Strellis, B., Bergin, M., Dibb, J., Picard, G., Libois, Q., Arnaud, L., et al.: Snow spectral albedo at Summit, Greenland: measurements and numerical simulations based on physical and chemical properties of the snowpack, The Cryosphere, 7, 1139–1160, 2013.

Chernyaev, E.: Marching cubes 33: Construction of topologically correct isosurfaces, Tech. rep., 1995.

Dang, C., Fu, Q., and Warren, S. G.: Effect of snow grain shape on snow albedo, Journal of the Atmospheric Sciences, 73, 3573–3583, 2016.

Dang, C., Zender, C. S., and Flanner, M. G.: Intercomparison and improvement of two-stream shortwave radiative transfer schemes in Earth system models for a unified treatment of cryospheric surfaces, The Cryosphere, 13, 2325–2343, 2019.

Déry, S. J. and Brown, R. D.: Recent Northern Hemisphere snow cover extent trends and implications for the snow-albedo feedback, Geophysical Research Letters, 34, 2007.

Dickinson, R. E.: Biosphere atmosphere transfer scheme (BATS) version 1e as coupled to the NCAR community climate model, NCAR Tech. Note TH-387+ STR, 1993.

Doherty, S., Warren, S., Grenfell, T., Clarke, A., and Brandt, R.: Light-absorbing impurities in Arctic snow, Atmospheric Chemistry and Physics, 10, 11 647–11 680, 2010.

Dumont, M., Brissaud, O., Picard, G., Schmitt, B., Gallet, J.-C., and Arnaud, Y.: High-accuracy measurements of snow Bidirectional Reflectance Distribution Function at visible and NIR wavelengths–comparison with modelling results, Atmospheric Chemistry and Physics, 10, 2507–2520, 2010.

Dumont, M., Brun, E., Picard, G., Michou, M., Libois, Q., Petit, J., Geyer, M., Morin, S., and Josse, B.: Contribution of light-absorbing impurities in snow to Greenland's darkening since 2009, Nature Geoscience, 7, 509–512, 2014.

Dumont, M., Flin, F., Malinka, A., Brissaud, O., Lapalus, P., Hagenmuller, P., Lesaffre, B., Dufour, A., Calonne, N., du Roscoat, S. R., et al.: Experimental and model based investigation of the links between snow bidirectional reflectance and snow microstructure, in: EGU General Assembly Conference Abstracts, p. 8744, 2017.

Dumont, M., Flin, F., Malinka, A., Brissaud, O., Hagenmuller, P., Lapalus, P., Lesaffre, B., Dufour, A., Calonne, N., Rolland du Roscoat, S., et al.: Experimental and model-based investigation of the links between snow bidirectional reflectance and snow microstructure, The Cryosphere, 15, 3921–3948, 2021.

Flanner, M. G. and Zender, C. S.: Linking snowpack microphysics and albedo evolution, Journal of Geophysical Research: Atmospheres, 111, 2006.

Flanner, M. G., Shell, K. M., Barlage, M., Perovich, D. K., and Tschudi, M.: Radiative forcing and albedo feedback from the Northern Hemisphere cryosphere between 1979 and 2008, Nature Geoscience, 4, 151–155, 2011.

Gardner, A. S. and Sharp, M. J.: A review of snow and ice albedo and the development of a new physically based broadband albedo parameterization, Journal of Geophysical Research: Earth Surface, 115, 2010.

Grenfell, T. C. and Perovich, D. K.: Radiation absorption coefficients of polycrystalline ice from 400–1400 nm, Journal of Geophysical Research: Oceans, 86, 7447–7450, 1981.

Grundy, W., Douté, S., and Schmitt, B.: A Monte Carlo ray-tracing model for scattering and polarization by large particles with complex shapes, Journal of Geophysical Research: Planets, 105, 29 291–29 314, 2000.

Hagenmuller, P., Chambon, G., Lesaffre, B., Flin, F., and Naaim, M.: Energy-based binary segmentation of snow microtomographic images, Journal of Glaciology, 59, 859–873, 2013.

Hagenmuller, P., Chambon, G., Flin, F., Morin, S., and Naaim, M.: Snow as a granular material: assessment of a new grain segmentation algorithm, Granular Matter, 16, 421–432, 2014.

Hagenmuller, P., Flin, F., Dumont, M., Tuzet, F., Peinke, I., Lapalus, P., Dufour, A., Roulle, J., Pézard, L., Voisin, D., et al.: Motion of dust particles in dry snow under temperature gradient metamorphism, The Cryosphere, 13, 2345–2359, 2019.

Hall, A.: The role of surface albedo feedback in climate, Journal of Climate, 17, 1550–1568, 2004.

Haussener, S., Gergely, M., Schneebeli, M., and Steinfeld, A.: Determination of the macroscopic optical properties of snow based on exact morphology and direct pore-level heat transfer modeling, Journal of Geophysical Research: Earth Surface, 117, 2012.

He, C. and Flanner, M.: Snow Albedo and Radiative Transfer: Theory, Modeling, and Parameterization, in: Springer Series in Light Scattering, pp. 67–133, Springer, 2020.

Hudson, S. R., Warren, S. G., Brandt, R. E., Grenfell, T. C., and Six, D.: Spectral bidirectional reflectance of Antarctic snow: Measurements and parameterization, Journal of Geophysical Research: Atmospheres, 111, 2006.

Hulst, H. C. and van de Hulst, H. C.: Light scattering by small particles, Courier Corporation, 1957.

Iaquinta, J., Isaka, H., and Personne, P.: Scattering phase function of bullet rosette ice crystals, Journal of Atmospheric Sciences, 52, 1401–1413, 1995.

Ishimoto, H., Adachi, S., Yamaguchi, S., Tanikawa, T., Aoki, T., and Masuda, K.: Snow particles extracted from X-ray computed micro-tomography imagery and their single-scattering properties, Journal of Quantitative Spectroscopy and Radiative Transfer, 209, 113–128, 2018.

Iwabuchi, H.: Efficient Monte Carlo methods for radiative transfer modeling, Journal of the atmospheric sciences, 63, 2324–2339, 2006.

Jacques, S. L.: Monte Carlo modeling of light transport in tissue (steady state and time of flight), in: Optical-thermal response of laser-irradiated tissue, pp. 109–144, Springer, 2010.

Jiao, Z., Ding, A., Kokhanovsky, A., Schaaf, C., Bréon, F.-M., Dong, Y., Wang, Z., Liu, Y., Zhang, X., Yin, S., et al.: Development of a snow kernel to better model the anisotropic reflectance of pure snow in a kernel-driven BRDF model framework, Remote Sensing of Environment, 221, 198–209, 2019.

Kaempfer, T. U., Hopkins, M., and Perovich, D.: A three-dimensional microstructure-based photon-tracking model of radiative transfer in snow, Journal of Geophysical Research: Atmospheres, 112, 2007.

Kokhanovsky, A. A. and Zege, E. P.: Scattering optics of snow, Applied Optics, 43, 1589–1602, 2004.

Letcher, T. W. and Minder, J. R.: Characterization of the simulated regional snow albedo feedback using a regional climate model over complex terrain, Journal of Climate, 28, 7576–7595, 2015.

Lewiner, T., Lopes, H., Vieira, A. W., and Tavares, G.: Efficient implementation of marching cubes' cases with topological guarantees, Journal of graphics tools, 8, 1–15, 2003.

665  Li, S. and Zhou, X.: Accuracy assessment of snow surface direct beam spectral albedo derived from reciprocity approach through radiative transfer simulation, in: IGARSS 2003. 2003 IEEE International Geoscience and Remote Sensing Symposium. Proceedings (IEEE Cat. No. 03CH37477), vol. 2, pp. 839–841, IEEE, 2003.

Libois, Q., Picard, G., France, J., Arnaud, L., Dumont, M., Carmagnola, C., and King, M.: Influence of grain shape on light penetration in snow, The Cryosphere, 7, 1803–1818, 2013.

670  Libois, Q., Picard, G., Dumont, M., Arnaud, L., Sergent, C., Pougatch, E., Sudul, M., and Vial, D.: Experimental determination of the absorption enhancement parameter of snow, Journal of Glaciology, 60, 714–724, 2014.

Libois, Q., Lévesque-Desrosiers, F., Lambert-Girard, S., Thibault, S., and Domine, F.: Optical porosimetry of weakly absorbing porous materials, Optics Express, 27, 22 983–22 993, 2019.

Liou, K., Takano, Y., and Yang, P.: Light absorption and scattering by aggregates: Application to black carbon and snow grains, Journal of
675  Quantitative Spectroscopy and Radiative Transfer, 112, 1581–1594, 2011.

Lorensen, W. E. and Cline, H. E.: Marching cubes: A high resolution 3D surface construction algorithm, ACM siggraph computer graphics, 21, 163–169, 1987.

Macke, A., Mueller, J., and Raschke, E.: Single scattering properties of atmospheric ice crystals, Journal of Atmospheric Sciences, 53, 2813–2825, 1996.

680  Malinka, A. V.: Light scattering in porous materials: Geometrical optics and stereological approach, Journal of Quantitative Spectroscopy and Radiative Transfer, 141, 14–23, 2014.

Mangan, A. P. and Whitaker, R. T.: Partitioning 3D surface meshes using watershed segmentation, IEEE Transactions on Visualization and Computer Graphics, 5, 308–321, 1999.

Natarajan, B. K.: On generating topologically consistent isosurfaces from uniform samples, The Visual Computer, 11, 52–62, 1994.

685  Neshyba, S. P., Grenfell, T. C., and Warren, S. G.: Representation of a nonspherical ice particle by a collection of independent spheres for scattering and absorption of radiation: 2. Hexagonal columns and plates, Journal of Geophysical Research: Atmospheres, 108, 2003.

Nielson, G. M. and Hamann, B.: The asymptotic decider: resolving the ambiguity in Marching Cubes., in: IEEE visualization, vol. 91, pp. 83–91, 1991.

Painter, T. H., Bryant, A. C., and Skiles, S. M.: Radiative forcing by light absorbing impurities in snow from MODIS surface reflectance
690  data, Geophysical Research Letters, 39, 2012.

Perovich, D. K.: Light reflection and transmission by a temperate snow cover, Journal of Glaciology, 53, 201–210, 2007.

Perovich, D. K. and Govoni, J. W.: Absorption coefficients of ice from 250 to 400 nm, Geophysical Research Letters, 18, 1233–1235, 1991.

Picard, G., Arnaud, L., Domine, F., and Fily, M.: Determining snow specific surface area from near-infrared reflectance measurements: Numerical study of the influence of grain shape, Cold Regions Science and Technology, 56, 10–17, 2009.

695  Picard, G., Libois, Q., and Arnaud, L.: Refinement of the ice absorption spectrum in the visible using radiance profile measurements in Antarctic snow, The Cryosphere, 10, 2655–2672, 2016.

Saito, M., Yang, P., Loeb, N. G., and Kato, S.: A novel parameterization of snow albedo based on a two-layer snow model with a mixture of grain habits, Journal of the Atmospheric Sciences, 76, 1419–1436, 2019.

Schroeder, W. J., Lorensen, B., and Martin, K.: The visualization toolkit: an object-oriented approach to 3D graphics, Kitware, 2004.

700  Scopigno, R.: A modified look-up table for implicit disambigua-tion of Marching Cubes, The visual computer, 10, 353–355, 1994.

Shi, T., Cui, J., Chen, Y., Zhou, Y., Pu, W., Xu, X., Chen, Q., Zhang, X., and Wang, X.: Enhanced light absorption and reduced snow albedo due to internally mixed mineral dust in grains of snow, Atmospheric Chemistry and Physics, 21, 6035–6051, 2021.

Skiles, S. M. and Painter, T. H.: Toward understanding direct absorption and grain size feedbacks by dust radiative forcing in snow with coupled snow physical and radiative transfer modeling, Water Resources Research, 55, 7362–7378, 2019.

705 Skiles, S. M., Painter, T. H., Deems, J. S., Bryant, A. C., and Landry, C. C.: Dust radiative forcing in snow of the Upper Colorado River Basin: 2. Interannual variability in radiative forcing and snowmelt rates, Water Resources Research, 48, 2012.

Skiles, S. M., Painter, T. H., Belnap, J., Holland, L., Reynolds, R. L., Goldstein, H. L., and Lin, J.: Regional variability in dust-on-snow processes and impacts in the Upper Colorado River Basin, Hydrological Processes, 29, 5397–5413, 2015.

Stamnes, K. and Stamnes, J. J.: Radiative transfer in coupled environmental systems: an introduction to forward and inverse modeling, John

710 Wiley & Sons, 2016.

Sullivan, C. B. and Kaszynski, A.: PyVista: 3D plotting and mesh analysis through a streamlined interface for the Visualization Toolkit (VTK), Journal of Open Source Software, 4, 1450, https://doi.org/10.21105/joss.01450, 2019.

Thackeray, C. W. and Fletcher, C. G.: Snow albedo feedback: Current knowledge, importance, outstanding issues and future directions, Progress in Physical Geography, 40, 392–408, 2016.

715 Theile, T. and Schneebeli, M.: Algorithm to decompose three-dimensional complex structures at the necks: tested on snow structures, IET Image Processing, 5, 132–140, 2011.

Van der Walt, S., Schönberger, J. L., Nunez-Iglesias, J., Boulogne, F., Warner, J. D., Yager, N., Gouillart, E., and Yu, T.: scikit-image: image processing in Python, PeerJ, 2, e453, 2014.

Verseghy, D. L.: CLASS—A Canadian land surface scheme for GCMs. I. Soil model, International Journal of Climatology, 11, 111–133,

720 1991.

Vionnet, V., Brun, E., Morin, S., Boone, A., Faroux, S., Moigne, P. L., Martin, E., and Willemet, J.-M.: The detailed snowpack scheme Crocus and its implementation in SURFEX v7. 2, Geoscientific Model Development, 5, 773–791, 2012.

Wang, X., Gillibert, L., Flin, F., and Coeurjolly, D.: Curvature-driven volumetric segmentation of binary shapes: an application to snow microstructure analysis, in: Proceedings of the 21st International Conference on Pattern Recognition (ICPR2012), pp. 742–745, IEEE,

725 2012.

Warren, S. G.: Can black carbon in snow be detected by remote sensing?, Journal of Geophysical Research: Atmospheres, 118, 779–786, 2013.

Warren, S. G. and Brandt, R. E.: Optical constants of ice from the ultraviolet to the microwave: A revised compilation, Journal of Geophysical Research: Atmospheres, 113, 2008.

730 Warren, S. G. and Wiscombe, W. J.: A model for the spectral albedo of snow. II: Snow containing atmospheric aerosols, Journal of Atmospheric Sciences, 37, 2734–2745, 1980.

West, B. A., Hodgdon, T. S., Parno, M. D., and Song, A. J.: Improved workflow for unguided multiphase image segmentation, Computers & geosciences, 118, 91–99, 2018.

Whitney, B. A.: Monte Carlo radiative transfer, in: Fluid Flows To Black Holes: A Tribute to S Chandrasekhar on His Birth Centenary, pp.

735 151–176, World Scientific, 2011.

Wiscombe, W. J.: Improved Mie scattering algorithms, Applied optics, 19, 1505–1509, 1980.

Wiscombe, W. J. and Warren, S. G.: A model for the spectral albedo of snow. I: Pure snow, Journal of Atmospheric Sciences, 37, 2712–2733, 1980.

Xiong, C., Shi, J., Ji, D., Wang, T., Xu, Y., and Zhao, T.: A new hybrid snow light scattering model based on geometric optics theory and

740 vector radiative transfer theory, IEEE Transactions on Geoscience and Remote Sensing, 53, 4862–4875, 2015.

Yang, P. and Liou, K.: Geometric-optics–integral-equation method for light scattering by nonspherical ice crystals, Applied Optics, 35, 6568–6584, 1996.